# Simulation study
# fluidization with heat transfer

Jegers, J.S.H.

*Award date:*
2017

Technische Universiteit
Eindhoven
University of Technology

**Process Engineering**

**Multiphase Reactor group (SMR)**

Department of Chemical Engineering and Chemistry

# Simulation study: fluidization with heat transfer

J.S.H. Jegers

August 30, 2016

**Author:**

J.S.H. Jegers (ID: 0747782)

**Graduation Committee:**

Prof. dr. ir. J.A.M. Kuipers (chair)

Dr. ir. J. van der Schaaf (external)

Prof. dr. ir. N.G. Deen (supervisor)

M. Banaei MSc. (tutor)

**Date:**

August 30, 2016

# Contents

# Abstract

Gas-solid fluidized bed reactors can be used in various processes like drying, catalytic cracking, polymerization and combustion. The main focus of this work is on polymerization reaction of polypropylene where Ziegler Natta catalyst is used. Polypropylene is used in a wide variety of products. As behavior of these reactors are complicated, some aspects of operation are open for further investigation.

In this work, analysis of such processes is purely done by simulation and two fluid model (TFM) based on the kinetic theory of granular flow (KGTF) is used. Also a novel technique for the implementation of tracer particles is tested for monitoring of solids mixing rate.

The main focus of this work is finding the effect of superficial gas velocity on hydrodynamics, heat transfer properties and mixing process of fluidized beds. This has been investigated on a 6cm diameter bed with an aspect ratio of 1. For this purpose velocities varying from 0.40 and 1.10m/s have been tested on a system which has a minimum fluidization velocity of 0.24m/s. In addition, some simulations have been performed for 12cm diameter beds to explore the scale effect in fluidized bed reactors. The TFM simulation results were compared to a similar research based on a discrete element method (DEM) simulation [1].

It was found that with an increase in superficial gas velocity more bubbles are formed and the emulsion phase shrinks. This leads to a more uniform solid temperature distribution throughout the bed. This behavior is a result of faster solids mixing. The same trend was observed in the study of the larger bed. The obtained results in the TFM are in good agreement with the DEM results.

Furthermore the effect of the restitution coefficient on the hydrodynamics and mixing rate was investigated. For this purpose restitution coefficient between 0.6 and 0.99 were used. It was found that, bubbles are more easily formed at relatively low restitution coefficient. In systems with high restitution coefficient (close to 1) bubble formation rarely occurs. However, particles are more spaciously coordinated as collision becomes more inelastic due to less energy dissipation from collisions.

# 1. Introduction

Nowadays pole-olefins are very popular products in various applications. This popularity is due to its (low) price, flexibility of molding and ease of disposal and recycling [2]. As a consequence 150 billion tons of polyethylene, polypropylene and polyolefins copolymers were manufactured in 2014 [3]. Production of these polyolefins can be executed in different chemical path ways, for example in a stirred tank reactor or in a fluidized bed.

Fluidized bed operation in combination with a Ziegler Natta catalyst is recognized as the most common operation method for the production of polyolefins. Although polyolefin production is operated for decades in this way, there are still some details in this process that are not completely understood [4]. These complexities are mainly about the hydrodynamics, heat and mass transfer properties of fluidized beds. Also the complex kinetics for a polyolefin reaction may take part in it [5].

A fluidized bed reactor is a vessel or contactor in which gas or liquid (fluid) is contacted with solid particles. A fluidized bed is formed when a fluid is passed upwards through a bed of particles and the friction force of the fluid on the particles balances the gravitational force. The minimum gas velocity that fluidization occurs is called minimum fluidization velocity.

A simplified process overview of fluidization is given in Figure 1. Gas (ethylene or propylene) are injected at the bottom of fluidized bed. Solids, in most of cases pre-polymerized particles, are fed at a higher level. Initially particles are small (light) enough for fluidization. As reaction proceeds, particles becomes larger and heavier, and they sink to the bottom of the reactor. In this way the product can be separated from the reactor. Unreacted gas is leaving the reactor at the top and it will be recycled.

Operation in a fluidized bed has many advantages comparing to other reactors; good heat transfer properties, good solid mixing and low pressure drop are some of them. As unreacted gas leaves the reactor at the top where the product is leaving at the bottom, there is no additional separation needed for the product. Operation in a fluidized bed has also some difficulties. For example, it is difficult to scale up these reactors as their behavior is complex.

Polyolefin reactions are extremely exothermic. Because the reaction rate at some spots could be higher than others, hotspots in the reactor may form. Since polyolefins have a relatively low melting point, particles tend to melt and might become sticky and as a result form an agglomerate. For this

reason, hotspots are undesired and can have a tremendous influence on the fluidization. Thus, the detection and the formation possibility of these hotspots have significant importance, and it play a key role in the further optimization of these processes.

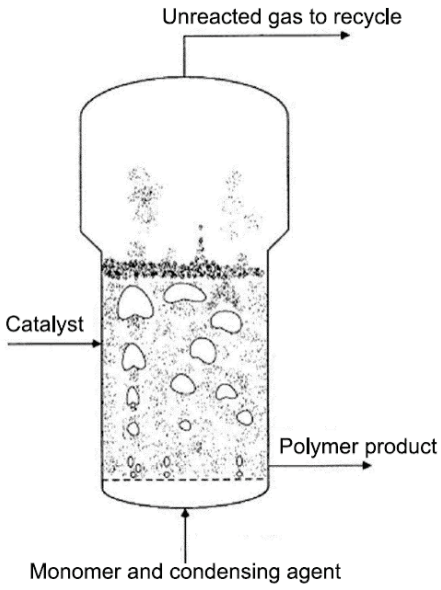


Figure 1: Process overview of polyolefin fluidized bed reactors [6]

In order to have a better understanding from hot-spot formation, effect of superficial gas velocity, size of the bed, and particle diameter are investigated in this study. This investigation is purely done by simulation using two fluid model (TFM) based on kinetic theory of granular flow (KTGF). This parameter study is the main goal of this project. Besides that, a new method for monitoring the solid mixing in fluidized beds is presented and carefully verified. Before starting such an important investigation, it was necessary to test and verify the developed two fluid model in-house code. Thus, some verification steps were also taken in this work.

In the next section, a brief overview of modeling techniques are presented. The governing equations for the TFM and the KTGF theory and the applied boundary conditions are given in chapter 2. In chapter 3 the verification of the code by several tests for the thermal energy solver is presented, completed with a sensitivity analysis. In Chapter 4, the simulation settings with respect to the used heat source, thermal operating window and initial conditions are discussed. In chapter 5 the final results of the effect of superficial gas velocity, bed size and particle diameter on solid temperature distribution are discussed. In chapter 6, a new method for monitoring solid mixing is introduced and thoroughly tested. The outcomes of this work is concluded in chapter 7 and it is completed with some recommendations.

# 2. Modeling

Depending on the scale of simulation, various models can be used. If fluid-particle interactions at small scale is the goal of research, direct numerical simulation (DNS) can be used. In the case that we are interested in the particle-particle interactions, we can use discrete particle modeling (DPM) (see Figure 2). As each interaction is calculated in these models, detailed information is obtained with the use of DNS or DPM simulations. The drawback of these models is their expensive computational time. For larger system, in which information on particle-particle interaction is less important, modeling can be done in a different way. For example, we can consider particulate phase as a fluid phase and use averaged continuity and averaged Navier-Stokes equations for them. In this way, we can capture the gas-solid interactions in the scale of computational grid cell. This model is called two fluid model (TFM). Modeling with the TFM is less time consuming than modeling with DPM or DNS. Consequently, it gives the possibility to model systems at large lab-scale within a quite reasonable computational time. For even larger scales (industrial scales: diameter up to 5 meters) discrete bubble modeling can be applied. In this modeling technique, bubbles are considered as discrete entities [7] and the emulsion phase behavior is predicted by averaged Navier-Stokes equations.

Within this research, the two fluid model has been used for fluidized beds at various scales to capture their heat transfer characteristics.

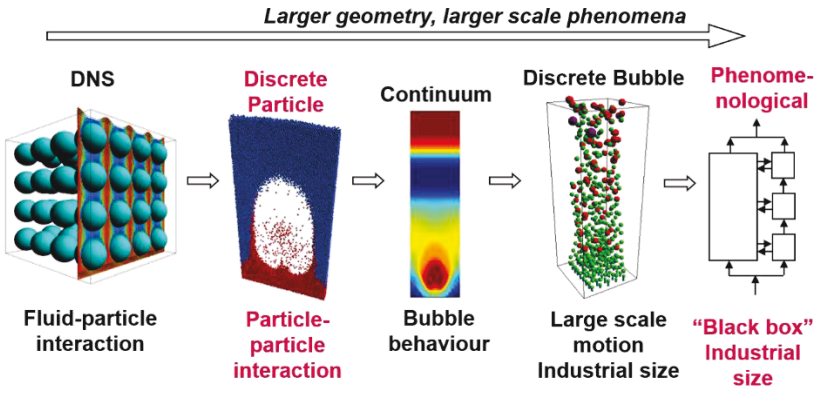


Figure 2: Overview modeling types

## 2.1 Governing equations

The two fluid model describes both phases in the fluidized bed reactor, gas and solid phases, as interpenetrating medium. In this model, the gas-solid interactions in the scale of computational grid cell are calculated by using generalized Navier-Stokes [8]. The model consist of three general sets of equations, continuity equation, the momentum conservation equations and the thermal energy balance. First the continuity equation is considered for both phases, given in (2.1) and (2.2).

$$\frac{\partial\left(\varepsilon_g\rho_g\right)}{\partial t}+\frac{1}{r}\frac{\partial}{\partial r}\left(r\varepsilon_g\rho_g u_{g,r}\right)+\frac{1}{r}\frac{\partial}{\partial\theta}\left(r\varepsilon_g\rho_g u_{g,\theta}\right)+\frac{\partial}{\partial z}\left(\varepsilon_g\rho_g u_{g,z}\right)=0 \qquad (2.1)$$

$$\frac{\partial\left(\varepsilon_s\rho_s\right)}{\partial t}+\frac{1}{r}\frac{\partial}{\partial r}\left(r\varepsilon_s\rho_s u_{s,r}\right)+\frac{1}{r}\frac{\partial}{\partial\theta}\left(r\varepsilon_s\rho_s u_{s,\theta}\right)+\frac{\partial}{\partial z}\left(\varepsilon_s\rho_s u_{s,z}\right)=0 \qquad (2.2)$$

In this equation, $\varepsilon$ corresponds to the void fraction of each phase, $\rho$ to the density (kg/m$^3$), $r,\theta,z$ are used in the cylindrical coordinate system for the radial, azimuthal and the axial directions respectively. Furthermore, the velocity of both phases (*i*) in each direction (*j*) are denoted with $u_{i,j}$ .

The second set of general equations are the momentum equations, these equations describe the variation of momentum for both phases and their interphase interactions. The momentum equations are given in (2.3) and (2.4). Contributing terms to this momentum equations are convection, pressure gradient force, viscous dissipation, interphase momentum exchange and gravitational forces. The extended version of this momentum equation can be found in Appendix A.

$$\frac{\partial\left(\varepsilon_g\rho_g\bar{u}_g\right)}{\partial t}+\nabla\cdot\left(\varepsilon_g\rho_g\overline{u_g}\,\overline{u_g}\right)=-\varepsilon_g\nabla P_g-\nabla\cdot\left(\varepsilon_g\overline{\overline{\tau_g}}\right)-\beta\left(\overline{u_g}-\overline{u_s}\right)+\varepsilon_g\rho_g\bar{g} \qquad (2.3)$$

$$\frac{\partial\left(\varepsilon_s\rho_s\overline{u_s}\right)}{\partial t}+\nabla\cdot\left(\varepsilon_s\rho_s\overline{u_s}\,\overline{u_s}\right)=-\varepsilon_s\nabla P_g-\nabla P_s-\nabla\cdot\left(\varepsilon_s\overline{\overline{\tau_s}}\right)+\beta\left(\overline{u_g}-\overline{u_s}\right)+\varepsilon_s\rho_s\bar{g} \qquad (2.4)$$

Where $\bar{u}$ is the velocity vector (m/s), $P_g$ and $P_s$ are the gas and solid pressure, $\tau$ is the stress tensor and $g$ is the gravitational acceleration. $\beta$ is defined as the interphase momentum transfer coefficient.

Besides the continuity and momentum equations a third set of general equations is needed to describe the thermal energy balance for both phases. Conductive and convective contribution is taken into account for both phases. For the solid phase a production term $\dot{q}$ (W/m$^3$) is also introduced that can mimic the exothermic nature of the polymerization reaction in a simple way. The general thermal equations for both gas and solid phases are given by (2.5) and (2.6).

$$C_{p,g}\frac{\partial(\varepsilon_g\rho_g T_g)}{\partial t}+C_{p,g}\nabla.\left(\varepsilon_g\rho_g\bar{u}_g T_g\right)=\nabla.\varepsilon_g k_g^{eff}\nabla T_g-h_{gs}(T_g-T_s) \tag{2.5}$$

$$C_{p,s}\frac{\partial(\varepsilon_s\rho_s T_s)}{\partial t}+C_{p,s}\nabla.\left(\varepsilon_s\rho_s\bar{u}_s T_s\right)=\nabla.\varepsilon_s k_s^{eff}\nabla T_s+h_{gs}(T_g-T_s)+\varepsilon_s\dot{q} \tag{2.6}$$

$C_p$ is the heat capacity (J/kg/K), $k_i^{eff}$ and $h_{gs}$ (2.11) are the thermal conductivity (W/m/K) and the interfacial heat transfer coefficient (W/m$^2$/K) for both phases respectively.

## 2.2 Closure equations

Besides the three governing equations that are described, some closure equations are needed to be able to solve them together. The first simple closure equation is the ideal gas law to correlate the gas density to local pressure (2.7).

$$\rho_g=\frac{M_g}{RT_g}P_g \tag{2.7}$$

in this equation, $M_g$ is the molecular weight of the gas and $R$ the universal gas constant ( $8.3145 J\cdot K^{-1}\cdot mol^{-1}$).

The second closure equation is used for the interphase momentum coefficient ( $\beta$ ), which can be obtained from drag force correlations ( $F_{drag}$ ). $\beta$ is used in both momentum equations (2.3) and (2.4) . And is given in equation (2.8):

$$\beta=\frac{F_{drag}\mu}{d_p{}^2} \tag{2.8}$$

in the dense regime ( $\varepsilon_g < 0.8$ ) the interphase momentum coefficient was calculated by using of the Ergun drag correlation (equation (2.9)) [9] and in the less dense area the interphase moment equation was computed by Wen and Yu correlation (equation (2.10)) [10].

$$F_{drag} = 150\frac{\left(1-\varepsilon_g\right)}{\varepsilon_g} + 1.75\varepsilon_g \,\mathrm{Re}_p \tag{2.9}$$

$$F_{drag}\,\frac{3}{4}C_D \,\mathrm{Re}_p \left(1-\varepsilon_g\right)\varepsilon_g^{-2.65} \tag{2.10}$$

in these equations, $\mathrm{Re}_p$ is the particle's Reynolds number and is given by equation (2.14)

Further closure equations have been used for calculation of the interfacial heat transfer coefficient This parameter is described as the form noted in (2.11). The $h_{gs}$ is calculated by using an empirical Gunn correlation. The mathematical form of this correlation is presented in equation (2.13) [11].

$$h_{gs} = \frac{6\cdot(1-\varepsilon_g)}{d_p}h_p \tag{2.11}$$

$$Nu_p = \frac{h_s d_p}{k_g} \tag{2.12}$$

$$Nu_p = \left(7-10\varepsilon_g+5\varepsilon_g^2\right)\left(1+0.7\,\mathrm{Re}_p^{0.2}\,\mathrm{Pr}^{0.33}\right)+\left(1.33-2.40\varepsilon_g+1.20\varepsilon_g^2\right)\mathrm{Re}_p^{0.7}\,\mathrm{Pr}^{0.33} \tag{2.13}$$

The Gunn correlation is a function of two dimensionless numbers: $\mathrm{Re}_p$ and $\mathrm{Pr}$ number, these are given (2.14) and (2.15) respectively.

$$\mathrm{Re}_p = \frac{\varepsilon_g \rho_g d_p \left(u_g - v_p\right)}{\mu_g} \tag{2.14}$$

$$\mathrm{Pr} = \frac{\mu_g C_{p,g}}{k_g} \tag{2.15}$$

The last set of closure equation is explained kinetic theory of granular flow (KTGF), and is explained in the next section.

## 2.3 Kinetic theory of granular flow

As mentioned earlier, in the two fluid model both gas and solid phase are two interpenetrating phases. For this purpose, the 'kinetic theory of granular flow (KTGF)' is used. This theory describes the dependence of solid rheology to the local solid concentration and the fluctuating motion of the particle due to its collisions. Hereby, the actual particle velocity, $c_s$ , is composed in the local mean velocity $u_s$ , and a random fluctuating component: $C_s$ , as in (2.16).

$$\overline{c_s} = \overline{u_s} + \overline{C_s} \tag{2.16}$$

This fluctuating component is analogues to the random motion of particles in gas. So, the granular temperature has been defined by (2.17)

$$\Theta = \frac{1}{3}\left\langle \overline{C_s} \cdot \overline{C_s} \right\rangle \tag{2.17}$$

where $\left\langle C_s \right\rangle$ is the averaged random fluctuation. The time dependency of the granular temperature is given by (2.18).

$$\frac{3}{2}\left[\frac{\partial}{\partial t}\left(\varepsilon_s \rho_s \theta\right) + \nabla \cdot \left(\varepsilon_s \rho_s \theta \overline{u_s}\right)\right] = -\left(p_s \bar{\bar{I}} + \varepsilon_s \overline{\overline{\tau_s}}\right) : \nabla \overline{u_s} - \nabla \cdot \left(\varepsilon_s q_s\right) - 3\beta\theta - \gamma \tag{2.18}$$

Within this function, $\bar{\bar{I}}$ is the unit tensor, $p_s$ the particle pressure, $q_s$ the pseudo-Fourrier fluctuating kinetic energy flux. More details about the derivation of this equation can be found in some related scientific books [12], [13] and in some research papers [14]–[16].

Within this work the constitutive equations of Nieuwland et al [16] are used (Table 1).

Table 1: KTGF Constitutive equations, by Nieuwland et al. 1996 [16]

Particle pressure:

$$P_s = \left[1 + 2(1+e_n)\varepsilon_s g_0\right]\varepsilon_s \rho_s \theta$$

Newtonian stress tensor (for solid phase, analogues for gas phase):

$$\overline{\overline{\tau_s}} = -\left[\left(\lambda_s - \frac{2}{3}\mu_s\right)\left(\nabla \cdot \overline{u_s}\right)\overline{\overline{I}} + \mu_s\left(\left(\nabla \overline{u_s}\right) + \left(\nabla \overline{u_s}\right)^T\right)\right]$$

Bulk viscosity:

$$\lambda_s = \frac{4}{3}\varepsilon_s \rho_s d_p g_0 \left(1+e_n\right)\sqrt{\frac{\theta}{\pi}}$$

Sheer viscosity

$$\mu_s = 1.01600\frac{5}{96}\pi\rho_s d_p \sqrt{\frac{\theta}{\pi}}\frac{\left(1+\frac{8}{5}\frac{(1+e_n)}{2}\varepsilon_s g_0\right)\left(1+\frac{8}{5}\varepsilon_s g_0\right)}{\varepsilon_s g_0} + \frac{4}{5}\varepsilon_s \rho_s d_p g_0 (1+e_n)\sqrt{\frac{\theta}{\pi}}$$

Pseudo-Fourrier fluctuating kinetic energy flux

$$\overline{q_s} = -\kappa_s \nabla \theta$$

Pseudo-thermal conductivity

$$\kappa_s = 1.02513\frac{75}{384}\pi\rho_s d_p \sqrt{\frac{\theta}{\pi}}\frac{\left(1+\frac{12}{5}\frac{(1+e_n)}{2}\varepsilon_s g_0\right)\left(1+\frac{12}{5}\varepsilon_s g_0\right)}{\varepsilon_s g_0} + 2\varepsilon_s \rho_s d_p g_0 (1+e_n)\sqrt{\frac{\theta}{\pi}}$$

Dissipation of fluctuating kinetic energy due to inelastic collisions

$$\gamma = 3\left(1-e_n^2\right)\varepsilon_s^2 \rho_s g_0 \theta\left[\frac{4}{d_p}\sqrt{\frac{\theta}{\pi}} - \left(\nabla \cdot \overline{u_s}\right)\right]$$

Radial distribution function solid phase (Ding and Gidaspow [15] ):

$$g_0 = \frac{3}{5}\left[1 - \left(\frac{\varepsilon_s}{\varepsilon_s^{\max}}\right)^{1/3}\right]^{-1} \qquad \text{with} \qquad \varepsilon_s^{\max} = 0.64356$$

## 2.4 Numerical method and boundary conditions

The equations that mentioned in previous chapter cannot be solved analytically, and they should be solved numerically. In this work, finite difference technique was used to solve all the equations. The interested reader is referred to the work by Goldschmidth [17] and Verma [18] for further details about the applied numerical approach.

The provided in house code is able to simulate cylindrical fluidized beds. Within this code a staggered grid configuration is used. This means, all the scalar variables (porosity, temperature, density, volume fractions and granular temperature) are stored in the cell centers, while the vector variables (velocities) are stored at the cell surfaces.

For solving all the equations, we also need to apply boundary conditions to some of the computational cells. Some of the boundary conditions that can be used in the model are listed in Table 2.

Table 2: Overview boundary conditions

| **Boundary conditions** |
|---|
| 1. Interior cell |
| 2. Free slip for gas and particles |
| 3. No-slip for gas and particles |
| 4. Prescribed influx for gas and particles |
| 5. Prescribed pressure for gas and permeable free-slip for particles |
| 6. Zero-gradient outflow for gas and particles |
| 7. No-slip for gas and partial slip for particles |
| 8. No-slip for gas and free-slip for particles |
| 9. Corner cell |
| 10. Prescribed pressure for gas and permeable no-slip for particles |
| 11. Periodic flow for gas and particles |

# 3. Verification

In order to verify the implemented two fluid model equations, various tests are performed and some of them are presented in this work. The main goal of these tests is to compare analytical solutions with the solution obtained by running the TFM code. The verification of hydrodynamics are presented by Verma [18] and only some of the verifications for thermal energy equations are presented in this work. Both conduction and convection terms were tested separately. These verifications are briefly presented in the next following sections. After verifying the code, grid and time-step sensitivity analysis were performed to find the right simulation settings in terms of time step and grid size. These analysis is also presented in this chapter.

## 3.1 Verification of conduction terms

The first verification test that is performed only captures the conduction heat transfer mechanism in a one-dimensional system. In this test, the superficial gas velocity is zero and there is no gas/solid flow. The bed has an initial temperature of 0 K and the bottom of the bed is hold at 0 K too. Constant heat is produced in every computational cell. Simulation have been performed for five seconds. Further details of the simulation are given in Table 3.

Table 3: simulation settings & condition conduction test

| **Simulation setting** | | |
|---|---|---|
| Number cells x-direction | 3 | - |
| Cell size x-direction | 5000 | m |
| Number cells azimuthal direction | 8 | - |
| Cell size azimuthal direction | 0.25 | m |
| Number of cells in vertical direction | 120 | - |
| Cell size vertical direction | 0.0030 | m |
| Time step | $5 \cdot 10^{-5}$ | s |
| Simulation time | 5 | s |
| **Simulation conditions** | | |
| Particle diameter | $9.875 \cdot 10^{-4}$ | m |
| Inlet gas temperature | 0 | K |
| Initial gas temperature | 0 | K |
| Initial solid temperature | 0 | K |
| Pressure | 101325 | Pa |
| Heat production | $1.4 \cdot 10^{7}$ | $W/m^3$ |
| Height | 0.36 | m |
| Superficial gas velocity | 0.0 | m/s |

Results were compared with the analytical solution given by (3.1) [19].

$$T_s = \left( a + \frac{k_s t \dot{q}}{\alpha} + \frac{\dot{q} x^2}{2\alpha} \right) \cdot erf\left( \frac{x}{2\sqrt{k_s t}} \right) + \frac{\dot{q} x}{\alpha} \left( \frac{k_s t}{\pi} \right)^{1/2} e^{-x^2/4k_s t} + bx - \frac{\dot{q} x^2}{2\alpha} \tag{3.1}$$

In which $a$ and $b$ are part of the initial temperature condition at time $t = 0$, equation (3.2).

$$T_s = ax + b \tag{3.2}$$

$x$ in this equation is the vertical position (m), $t$ is the time (s), $\dot{q}$ is the volumetric heat production (W/m$^3$), $\alpha$ the thermal diffusivity (m$^2$/s) given by (3.3), $k_s$ the thermal conductivity (W/m/K), $\rho_s$ the solid density (kg/m$^3$) and $C_{p,s}$ the solid heat capacity (J/kg/K).

$$\alpha = \frac{k_s}{\rho C_{p,s}} \tag{3.3}$$

The comparison between simulation results and analytical solution is presented in Figure 3. As can been seen in the graph, both results are in good agreement with each other. With evolving times, the temperature of the bed becomes higher as more heat is produced. The bed is only cooled at the bottom therefore at certain heights a steady temperature profile is established. It can be concluded that the conduction part of the model works well.

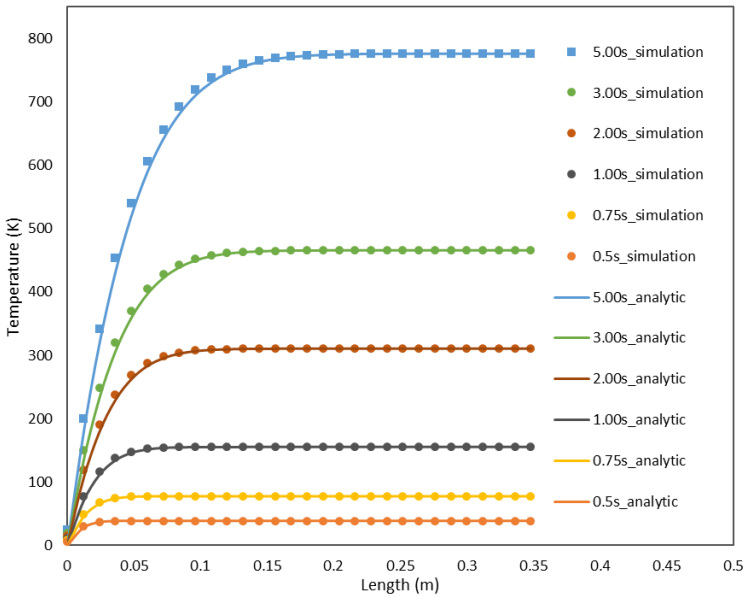


Figure 3: Conduction verification; solid temperature as function of height at varying simulation times.

## 3.2 Verification of convection terms

The second test case was performed for verification of the convection terms (in one –dimension) in the two fluid model. Therefore, a fixed bed was simulated in which the conduction part was turned off. Within this test, the 'flow-solver' was turned off too. The only captured heat transfer mechanism is convection.

The initial temperature of the bed was set to 300K for both phases. The temperature of the incoming gas was set to 200K and a uniform velocity profile was applied. As a boundary condition, the temperature at the bottom for both phases was set to 200K. Further details of this verification test are given in Table 4.

Table 4: Simulation settings & conditions convection in a fixed bed

| **Simulation setting** | | |
|---|---|---|
| Number cells x-direction | 3 | - |
| Cell size x-direction | 100 | m |
| Number cells azimuthal direction | 8 | - |
| Cell size azimuthal direction | 0.25 | m |
| Number of cells in vertical direction | 300 | - |
| Cell size vertical direction | 0.0012 | m |
| Time step | $8 \cdot 10^{-4}$ | s |
| Simulation time | 4 | s |
| **Simulation conditions** | | |
| Particle diameter | $9.875 \cdot 10^{-4}$ | m |
| Inlet gas temperature | 200 | K |
| Initial gas temperature | 300 | K |
| Initial solid temperature | 300 | K |
| Pressure | 101325 | Pa |
| Heat production | $1.4 \cdot 10^{7}$ | $W/m^3$ |
| Height fixed bed | 0.36 | m |
| Porosity fixed bed | 0.5 | $m^3_{bed}/m^3_{reactor}$ |
| Superficial gas velocity | 0.5 | m/s |

The results that were obtained by simulation were compared with results coming from a one-dimensional fixed bed model. The heat balances for this model are given in respective equation (3.4) and (3.5) for the gas and solid phase. Results were deducted from these equation by discretizing (first order-upwind) this set of equation before they were solved in MATLAB. The derivation for these discretized forms can be found in appendix B.

$$\varepsilon_g C_{p,g} \rho_g \frac{\partial T_g}{\partial t} = -u_z \varepsilon_g C_{p,g} \rho_g \frac{\partial T_g}{\partial z} + h_s a_s \left( T_s - T_g \right) \tag{3.4}$$

$$\varepsilon_s C_{p,p} \rho_p \frac{\partial T_s}{\partial t} = h_s a_s \left( T_g - T_s \right) + \varepsilon_s \dot{q}_p \tag{3.5}$$

$$a_s = 6 \frac{(1-\varepsilon_g)}{d_p} \tag{3.6}$$

In which $\varepsilon_i$ is the volume fraction for both gas and solid phase, $C_p$ is the heat capacity (J/kg/K), $\rho$ is the density, $h$ the heat transfer coefficient (W/m$^2$/K), $a_s$ the specific area given by (3.6), $u_z$ the superficial gas velocity (m/s) and $T_g$ / $T_p$ are the gas and solid temperature (K) respectively.

Both results, gas temperature and solid temperature for simulation and the fixed bed model are visualized in Figure 4 (gas temperature) and Figure 5 (solid temperature). A trend that in both gas and solid results is observed in the moving 'cooling-front' as result of the inflow of cold gas. The goal of this verification test was to check whether the simulation results are comparable with the fixed bed model results. It can be deducted from both figures, Figure 4 and Figure 5, the simulation results are in very good agreement with the model results. So, it was concluded that the convection terms in the in-house code were implemented properly.

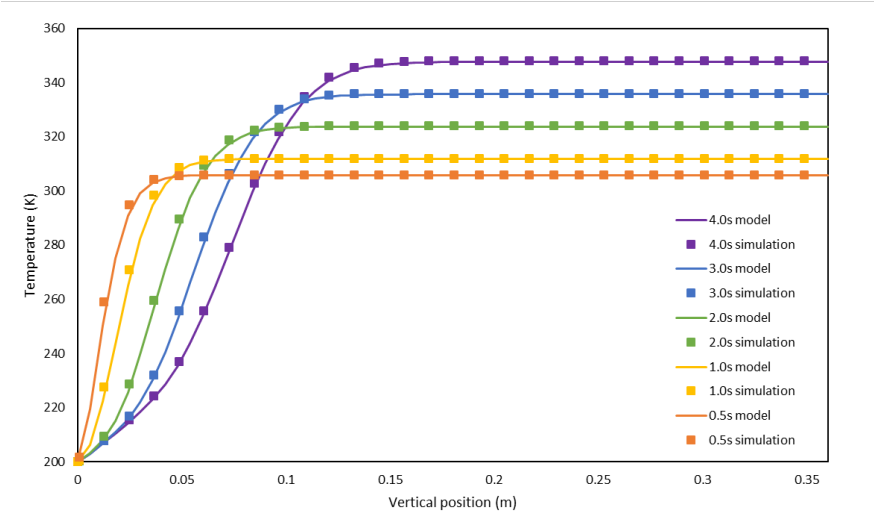


Figure 4: Gas temperature as function of vertical position in the reactor.

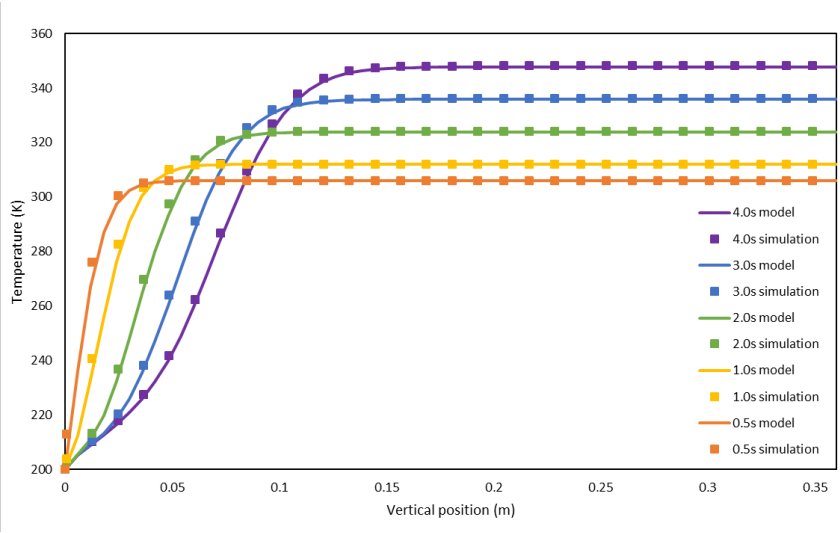


Figure 5: Solid temperature fixed bed verification test

## 3.3 Grid size sensitivity analysis

Before running simulation it is necessary to check in what extend simulation results will be dependent on the chosen grid size. These tests set criteria for the simulations that have to be performed. Several test have been performed with different number of grid cells and grid sizes. In this way, simulation will be accurate enough and not unnecessary big. This latter in favor of the simulation time. A cylindrical fluidized bed is considered, this means sensitivity tests have been performed in axial, radial and azimuthal direction. The dimensions of the bed and the simulation conditions were kept constant, and they are listed in Table 5. Particle properties that have been used in these simulations are listed in Table 12.

Table 5: Simulation setting and condition grid cell sensitivity tests.

| **Simulation setting** | | |
|---|---|---|
| Radius | 0.032 | m |
| Height | 0.120 | m |
| Time step | $8 \cdot 10^{-6}$ | s |
| Simulation time | 5 | s |
| **Simulation conditions** | | |
| Particle diameter | $9.875 \cdot 10^{-4}$ | m |
| Inlet gas temperature | 324 | K |
| Initial gas temperature | 200 | K |
| Initial solid temperature | 200 | K |
| Pressure | 101325 | Pa |
| Heat production | 0.0 | $W/m^3$ |
| Aspect ratio | 1 | - |
| Porosity fixed bed | 0.4 | $m^3_{bed}/m^3_{reactor}$ |
| Superficial gas velocity | 0.8 | m/s |

An overview of the performed grid size sensitivity tests in axial direction is given in Table 6. Seven cases have been tested, in which case D is the reference case and is used also in the radial and azimuthal direction. Results for the gas and solid temperature in respect with time are given in Figure 6 and Figure 7.

Table 6: overview axial grid refinement simulations

| | Case A | Case B | Case C | Case D reference | Case E | Case F | Case G |
|---|---|---|---|---|---|---|---|
| Radial cells | 8 | | | | | | |
| Radial Cell size (m) | 0.004 | | | | | | |
| Azimuthal cells | 32 | | | | | | |
| Azimuthal cell size (m) | 0.0625 | | | | | | |
| Axial cells | 120 | 80 | 60 | 40 | 30 | 20 | 15 |
| Axial cell size (m) | 0.001 | 0.0015 | 0.002 | 0.003 | 0.004 | 0.006 | 0.008 |

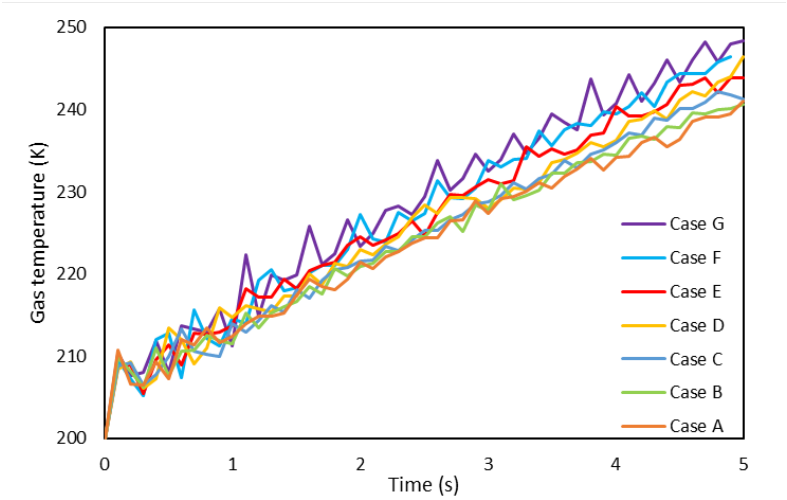


Figure 6: Gas temperature axial grid refinement, Case A until G

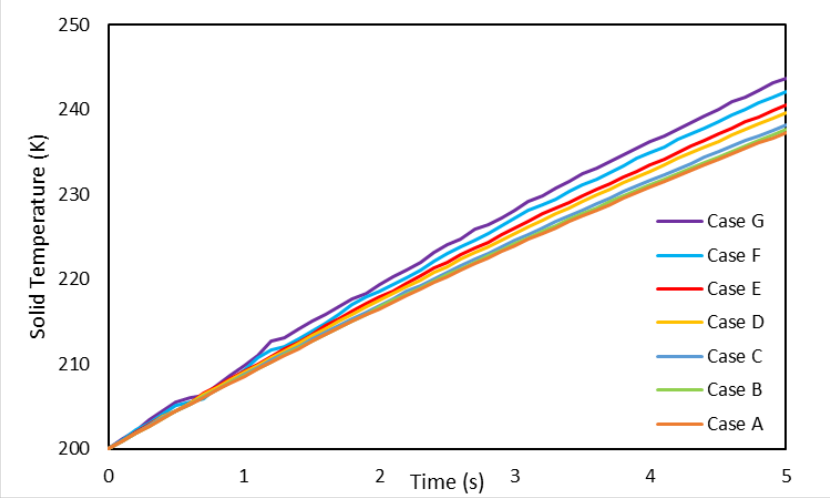


Figure 7: Solid temperature axial grid refinement

As can be observed from Figure 6 and Figure 7, simulation with an increased number of grid cells tend to give decrease in temperature. Also, Case A, Case B and Case C tend to go to the same solution, the deviation between these simulations is negligible. This indicates, in the mention cases a sufficient number of grid cells was applied. Another observation, in Figure 6, is that the fluctuation of the gas temperature become lower with an increase of the number of grid cells.

In radial direction six different simulation cases were performed, an overview of these cases is given in Table 7. Results of average gas and solid temperature profiles in time are given in Figure 8 and Figure 9 respectively. Simulation conditions for all of these cases are listed in Table 5.

Table 7: overview radial grid refinement simulations

| | **Case H** | **Case I** | **Case J** | **Case D reference** | **Case K** | **Case L** |
|---|---|---|---|---|---|---|
| Radial cells | 20 | 16 | 10 | 8 | 5 | 4 |
| Radial Cell size (m) | 0.0016 | 0.002 | 0.0032 | 0.004 | 0.0064 | 0.008 |
| Azimuthal cells | | | | 32 | | |
| Azimuthal cell size (m) | | | | 0.0625 | | |
| Axial cells | | | | 40 | | |
| Axial cell size (m) | | | | 0.003 | | |

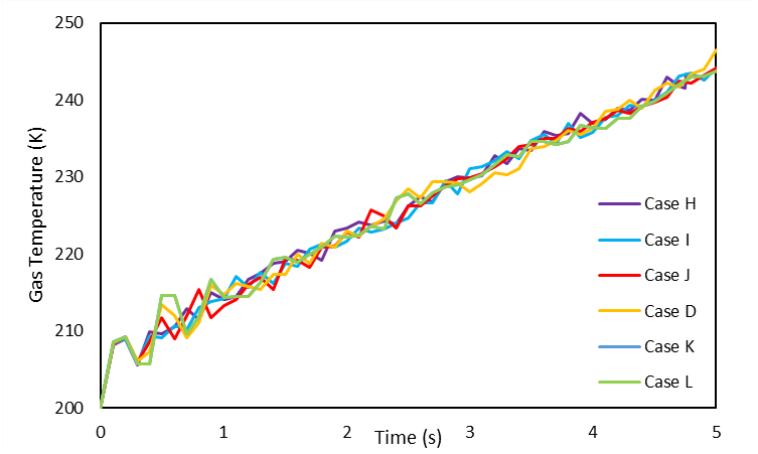


Figure 8: Gas temperature radial grid refinement

As can be seen from Figure 8 and Figure 9 grid refinement in the radial direction does not have a significant influence on the results. There is almost no distinction between the results six performed simulations. This indicates that for these simulations a sufficient number of grid cells was applied.

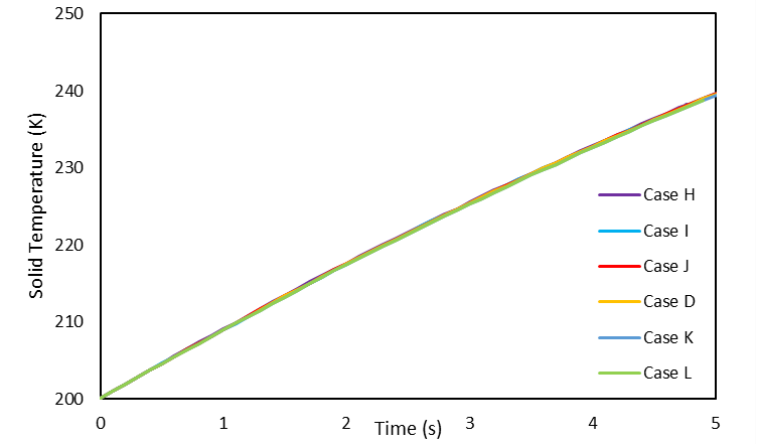


Figure 9: Solid temperature radial grid refinement

Also in azimuthal direction sensitivity analysis have been performed, in this direction five different cases were performed. An overview of these cases is given in Table 8. Simulation conditions for these cases are listed in Table 5. Results for these cases are presented in Figure 10 and Figure 11.

Table 8: overview azimuthal grid refinement simulations

| | **Case M** | **Case N** | **Case D reference** | **Case O** | **Case P** |
|---|---|---|---|---|---|
| Radial cells | | | 8 | | |
| Radial Cell size (m) | | | 0.004 | | |
| Azimuthal cells | 50 | 40 | 32 | 20 | 16 |
| Azimuthal cell size (m) | 0.04 | 0.05 | 0.0625 | 0.1 | 0.125 |
| Axial cell | | | 40 | | |
| Axial cell size (m) | | | 0.003 | | |

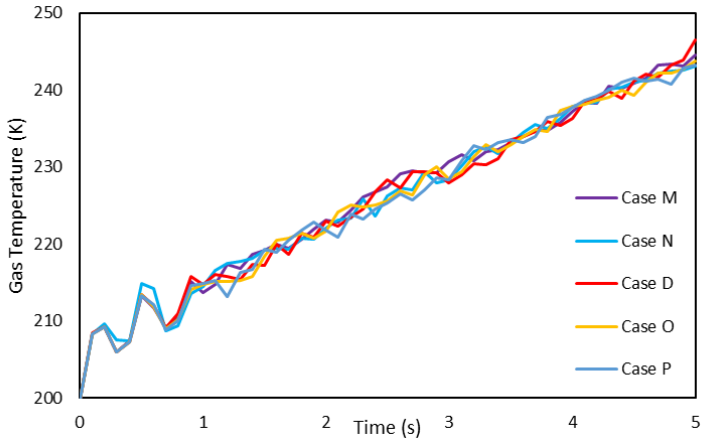


Figure 10: Gas temperature azimuthal grid refinement

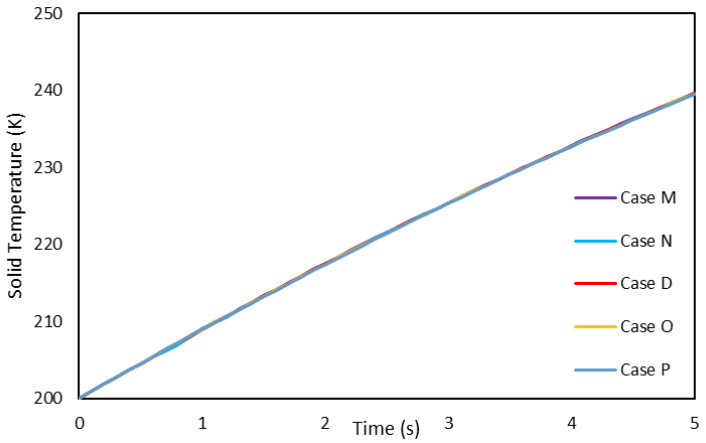


Figure 11: Solid temperature azimuthal grid refinement

As can be deduced from Figure 10 and Figure 11, and earlier grid sensitivity results, also in this direction a sufficient number of cell is being used during these simulations. With a change in number of cells in the azimuthal direction, no significant change in average temperature evolution was observed.

To summarize, the simulation results showed that average temperature evolution is more sensitive to the axial grid size than azimuthal and radial grid size. It is also observed that the grids with *dz = 2-3* times $d_p$ or smaller can give an independent result and this restriction should be considered in all the simulations.

## 3.4 Time step sensitivity analysis

In order to test the two fluid model for its sensitivity to time step, several test have been performed with various time steps. The total time of the simulation was kept constant. The purpose of this test is to test sensitivity of the results to time step and also to determine a suitable time step for simulations. Simulation conditions for these tests are listed in Table 9.

Table 9: Simulation settings and condition time step sensitivity tests

| **Simulation setting** | | |
|---|---|---|
| Number cells x-direction | 6 | - |
| Cell size x-direction | 0.0050 | m |
| Number cells azimuthal direction | 32 | - |
| Cell size azimuthal direction | 0.0625 | m |
| Number of cells in vertical direction | 60 | - |
| Cell size vertical direction | 0.0040 | m |
| Simulation time | 5 | s |
| **Simulation conditions** | | |
| Particle diameter | $9.875 \cdot 10^{-4}$ | m |
| Inlet gas temperature | 324.0 | K |
| Initial gas temperature | 328.8 | K |
| Initial solid temperature | 329.5 | K |
| Pressure | 101325 | Pa |
| Heat production | $6.7 \cdot 10^{5}$ | $W/m^3$ |
| Superficial gas velocity | 1.0 | m/s |

In total five different time steps were tested, listed in Table 10. Initially, one simulation with larger time-step was also tested but the code was not able to converge and run. The spatial-average gas and solid temperatures that obtained from these simulations are presented in Figure 12 and Figure 13 respectively.

Table 10: Overview time sensitivity tests

| | **Case Q** | **Case R** | **Case S** | **Case T** | **Case U** |
|---|---|---|---|---|---|
| Time step (s) | $1 \cdot 10^{-6}$ | $5 \cdot 10^{-6}$ | $7.5 \cdot 10^{-6}$ | $1 \cdot 10^{-5}$ | $5.0 \cdot 10^{-5}$ |
| Number of steps | $5 \cdot 10^{6}$ | $1 \cdot 10^{6}$ | $6.67 \cdot 10^{5}$ | $5 \cdot 10^{5}$ | $1 \cdot 10^{5}$ |

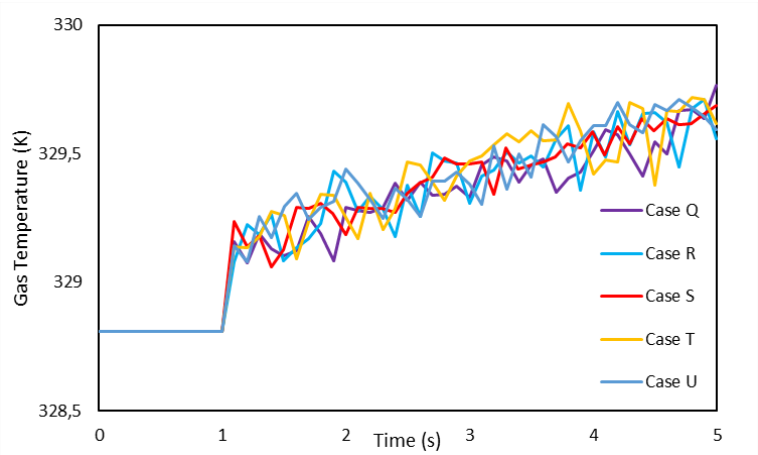


Figure 12: Gas temperature with varying time steps

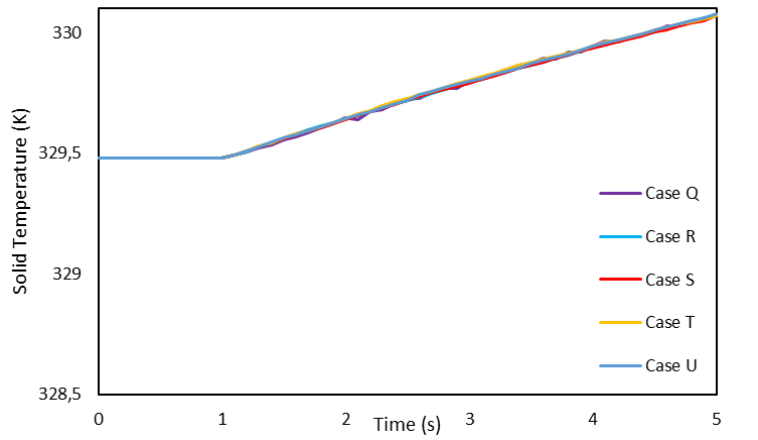


Figure 13: Solid temperature with varying time steps

As can be seen from both figures, no major difference between the results of performed simulations can be observed. As noted before, too large time step can make the simulation unstable in a way that convergence cannot be reached within the margins. Therefore, time step of $1 \cdot 10^{-5}$ s or smaller was chosen for all the performed simulations in this work.

# 4. Simulation conditions

Before starting the simulation, several parameters were needed to be determined. These parameters are heat production rate and the thermal steady state temperature in in poly-olefin production reactors. In this chapter, the procedure for calculation of these parameters and their final values are presented and discussed.

## 4.1 Heat source

There are several methods available for modeling the heat source of polyolefin reaction. One option is implementation of kinetics in the two fluid model [20] [21] but in this work a simpler approach was used. In this project, a constant heat source is used to mimic the heat production by reaction. This volumetric heat source, $\dot{q}$ (W/m$^3$) in equation (2.6) is constant for the solid phase. This implies that all the particles should be uniform in shape, dimensions and catalytic activity. It also implies that all the particles experience the same condition. The magnitude of this volumetric heat source was determined using different sources, [2] [1] [22]. In [2] a relatively simple expression (4.1) for the reaction rate is purposed for polypropylene particles with a diameter $d_p$ of $10^{-3}$m, comparable with simulation done in this work.

$$R_p = k_{p0} \exp\left(\frac{-E_a}{RT_p}\right) \cdot w_c P_r \tag{4.1}$$

$R_p$ in this expression is the reaction rate, $k_{p0}$ is the pre-exponential factor of the polymerization rate coefficient, $E_a$ is the activation energy, $R$ the gas coefficient, $T_p$ the particle temperature, $w_c$ the catalyst concentration and $P_r$ the reactor pressure. When using the values noted in Table 11, a volumetric heat source was found of $8.60 \cdot 10^5$W/m$^3$ was found. It must be mentioned, the reaction rate increases linearly with pressure and the operating pressure in [2] is 31atm. This however, gives an estimation for the order of magnitude of the heat source term.

Table 11: Reaction rate values used in [2]

| Reaction rate constants | | |
|---|---|---|
| $k_{po}$ | $8.948 \cdot 10^{-6}$ | kg PP/s/Pa/kg-cat |
| $E_a$ | 10585 | J/mol |
| $R$ | 8,3145 | J/K/mol |
| $T_p$ | 330 | K |
| $w_c$ | $7.0 \cdot 10^{-7}$ | kg/m$^3$ |
| $p_r$ | $3.1 \cdot 10^6$ | Pa |
| $\Delta H_r$ | 2510 | J/kg |

In [1] the effect of superficial gas velocity on the particle temperature distribution has been investigated, for this purpose, also a constant volumetric heat source has been used to mimic the heat production. In this specific investigation for polypropylene particles with a diameter of $9.875 \cdot 10^{-4}$m two different thermal heat sources have been used, $6.7 \cdot 10^5$ W/m$^3$ and $1.31 \cdot 10^6$W/m$^3$. This data in this research was used to simulate fluidized bed operation at a pressure of 1atm.

In [22] information on reaction rate is provided for a Ziegler-Natta catalyzed polymerization with 50-70 g polypropylene/g catalyst/hour. The investigation was performed under atmospheric pressure. With using 2400J/kg polyethylene heat of reaction, heat source of $4.65 \cdot 10^5$ W/m$^3$ was found.

For this research, the magnitude of the thermal heat source has been chosen to be $6.7 \cdot 10^5$W/m$^3$ as used by [1], specifications in this research are comparable with their work. Other particle and gas properties are given in Table 12. Particles with this specification will behave like Geldart B particles [23].

Table 12: Physical properties for gas and solid phases used in the two fluid simulations [1], [2]

| **Physical properties gas and solid phase** | | | |
|---|---|---|---|
| Solid density | $\rho_s$ | 667 | kg/m$^3$ |
| Heat capacity solid | $C_{p,s}$ | 1670 | J/kg/K |
| Heat capacity gas | $C_{p,\mathrm{g}}$ | 1670 | J/kg/K |
| Molecular weight gas | $M_{w,gas}$ | $4.208 \cdot 10^{-2}$ | kg/mol |
| Kinematic viscosity | $\mu_g$ | $1 \cdot 10^{-5}$ | Pa·s |
| Initial solid conductivity | $k_{s,o}$ | $2.09 \cdot 10^{-2}$ | J/m/K |
| Heat source | $\dot{q}$ | $6.7 \cdot 10^5$ | W/m$^3$ |
| Particle diameter | $d_p$ | $9.8750 \cdot 10^{-4}$ | m |
| Minimum fluidization velocity[1] | $u_{mf}$ | 0.2455 | m/s |
| Gravitational acceleration | $g$ | 9.81 | m$^2$/s |

## 4.2 Polymer softening

Mechanical properties of polymers change with an increase in temperature. At elevated temperature this results in enhanced adhesion tendencies [24]. At relatively high temperatures, the polymers' chain become more mobile and their crystallinity decreases. Due to these effects, the young's modulus of polymers and therefore their deformation resistance decreases with temperature. Within fluidized bed operations, particles collide to each other continuously. If the young modulus becomes lower than a certain value, significant deformation can occur, contact surface increases, consequently collisions take more time, and the probability of agglomeration increases. These phenomena happen above a certain temperature. This temperature is called softening temperature. The softening temperature depends on several factors like polymer molecular weight and crystallinity.

The softening temperature that was found for polyethylene is about 373K, this is for LDPE, with a crystallinity fraction of 0.5 [24]. It was found the softening temperature for polypropylene is slightly higher, 393K [25] [26]. These properties limit the thermal operating window for polymerization reaction and should be taken into account during simulations.

[1] Minimum fluidization velocity is determined under atmospheric pressure, at a 324K, and the given particle diameter.

## 4.3 Continuously stirred tank reactor assumption

For investigating the effect of various parameters on heat transfer properties, it is necessary to perform all simulations at their thermal steady state condition. Determination of the steady state thermal conditions is a time consuming job. A few seconds of simulation can take several weeks. Performing long simulations for finding their thermal steady state condition is not a pragmatic option. Simple, wise and adequate assumptions have to be made to find out these conditions.

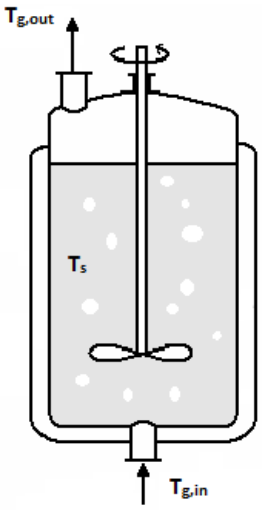

Figure 14: CSTR schematic

A very basic assumption is that a fluidized bed behaves like a (two-phase) continuous stirred tank reactor when it comes to heat transfer. The first estimation for the initial temperature of the reactor was made in this manner. Equations for this assumptions are given in (4.2) and (4.3). In Figure 14 a schematic representations is given for this CSTR.

$$\varepsilon_g \rho_g c_{p,g} V \frac{dT_g}{dt} = u_g A \rho_g c_{p,g} \left( T_{g,in} - T_g \right) + h_s \, a_s \, V \left( T_p - T_g \right) \tag{4.2}$$

$$\varepsilon_s \rho_s c_{p,s} V \frac{dT_s}{dt} = h_s \, a_s \, V \left( T_g - T_p \right) + \varepsilon_s V \dot{q} \tag{4.3}$$

The gas phase is described as a continuous phase with a superficial gas velocity, $u_g$, (m/s) whereas the solid phase is described as a fraction of the bed in which heat is produced. The volumetric heat production term, $\dot{q}$, (W/m$^3$) is used to mimic the heat of reaction. $h_s$ is the heat transfer coefficient (W/m$^2$/K) describing the heat transfer between both phases. $a_s$ (3.6) is the specific area (m$^{-1}$) for the solid particles. $V$ and $A$ the volume and the (inflow) surface of the reactor. ρ

These equations ((4.2) and (4.3)), and their discretized forms (see appendix C) are used to find the first guess of steady state temperature in the fluidized bed. After solving the discretized form of these equations, it is possible to find the temperatures evolution and their steady state values. Simulations with these initial guesses were performed. After a few seconds of simulation, the average gas and solid temperature and their evolution were obtained. If these gas or solid temperature were increasing or decreasing with time, the simulations were restarted with new initial conditions. To do so, we needed to correct our guesses for initial temperatures. In the first step, the temperature evolution was

obtained from TFM results. After that, the parameters in CSTR discretized equations were changed in a way that similar temperature trend could be obtained. It should be noted that, we found the bed height after performing the simulations with TFM and this parameter can be directly used in CSTR equations. On the other hand, the void fraction and interfacial heat transfer coefficient were adjusted. This procedure were repeated multiple times to achieve a thermal steady state condition. After doing this procedure for all the desired simulations, their thermal steady-state condition were obtained and these results are presented in Table 13.

Table 13: Results CSTR assumption for simulations.

| **Effect of superficial velocity 6cm bed** | | | |
|---|---|---|---|
| Case A | $u_g = 0.4(m/s)$ | $T_{s,0} = 337.63(K)$ | $T_{g,0} = 337.32(K)$ |
| Case B | $u_g = 0.5(m/s)$ | $T_{s,0} = 335.59(K)$ | $T_{g,0} = 335.29(K)$ |
| Case C | $u_g = 0.6(m/s)$ | $T_{s,0} = 334.35(\mathrm{K})$ | $T_{g,0} = 334.05(K)$ |
| Case D | $u_g = 0.7(m/s)$ | $T_{s,0} = 333.25(\mathrm{K})$ | $T_{g,0} = 332.94(K)$ |
| Case E | $u_g = 0.8(m/s)$ | $T_{s,0} = 332.68(K)$ | $T_{g,0} = 332.36(K)$ |
| Case F | $u_g = 0.9(m/s)$ | $T_{s,0} = 332.09(K)$ | $T_{g,0} = 331.73(K)$ |
| Case G | $u_g = 1.0(m/s)$ | $T_{s,0} = 331.59(K)$ | $T_{g,0} = 331.19(K)$ |
| Case H | $u_g = 1.1(m/s)$ | $T_{s,0} = 331.06(K)$ | $T_{g,0} = 330.72(K)$ |
| **Effect of superficial velocity 12cm bed** | | | |
| Case A | $u_g = 0.4(m/s)$ | $T_{s,0} = 355.33(K)$ | $T_{g,0} = 355.11(K)$ |
| Case B | $u_g = 0.5(m/s)$ | $T_{s,0} = 350.30(K)$ | $T_{g,0} = 350.06(K)$ |
| Case C | $u_g = 0.6(m/s)$ | $T_{s,0} = 347.25(K)$ | $T_{g,0} = 346.88(K)$ |
| Case D | $u_g = 0.7(m/s)$ | $T_{s,0} = 344.83(\mathrm{K})$ | $T_{g,0} = 344.46(K)$ |
| Case E | $u_g = 0.8(m/s)$ | $T_{s,0} = 342.79(\mathrm{K})$ | $T_{g,0} = 342.39(K)$ |
| Case F | $u_g = 0.9(m/s)$ | $T_{s,0} = 341.34(K)$ | $T_{g,0} = 340.97(K)$ |
| Case G | $u_g = 1.0(m/s)$ | $T_{s,0} = 340.07(K)$ | $T_{g,0} = 339.62(K)$ |
| Case H | $u_g = 1.1(m/s)$ | $T_{s,0} = 338.06(K)$ | $T_{g,0} = 337.72(K)$ |
| **Effect of particle diameter** | | | |
| Case A | $d_p = 4.937 \cdot 10^{-4}(m)$ | $T_{s,0} = 327.35(K)$ | $T_{g,0} = 327.13(K)$ |
| Case B | $d_p = 9.875 \cdot 10^{-4}(m)$ | $T_{s,0} = 327.19(\mathrm{K})$ | $T_{g,0} = 326.83(K)$ |
| Case C | $d_p = 1.234 \cdot 10^{-3}(m)$ | $T_{s,0} = 327.13(\mathrm{K})$ | $T_{g,0} = 326.76(K)$ |
| Case D | $d_p = 1.481 \cdot 10^{-3}(m)$ | $T_{s,0} = 327.11(K)$ | $T_{g,0} = 326.75(K)$ |

# 5. Results

Numerous successful researches have been done on the hydrodynamics of fluidized beds and at various (simulation) scales. For example, some specific researches on two-fluid-scale were done by [8][27][28][29]. They found that larger superficial gas velocities results in higher void fractions. It is also shown that particle interaction play a large role in the heat transfer [20]. One of these researches were conducted with discrete element model (DEM) to investigate the effect of superficial gas velocity on heat transfer and temperature distribution in polyolefin reactors [22]. They found that the particles' temperature becomes more homogenous with increasing superficial gas velocity [1]. It was also claimed that the average heat transfer coefficient is independent of superficial gas velocity [1]. Similar investigations were made to compare the results of TFM with DEM. This comparison can give us a better insight on the accuracy of TFM as DEM has less assumptions than TFM. These investigations, their results and further studies and analysis are presented in the next following sections.

## 5.1 Effect of superficial gas velocity on hydrodynamics

In this section, the effect of superficial gas velocity and comparison between TFM and DEM results are presented. For this purpose, velocities varying from 0.4 – 1.1 m/s are tested. Simulation setting and conditions are listed in Table 14. Conditions listed in this table are kept constant for all simulations. Time step and grid size parameters have been chosen in agreement with the executed sensitivity analysis in chapter 3.

Table 14: Simulation setting and condition velocity simulations

| **Simulation conditions** | | |
|---|---|---|
| Bed diameter | 0.06 | m |
| Bed height | 0.06 | m |
| Aspect ratio | 1 | - |
| Void fraction | 0.6 | - |
| Particle diameter | $9.875 \cdot 10^{-4}$ | m |
| Inlet gas temperature | 324 | K |
| Pressure | 101325 | Pa |
| Heat production | $6.7 \cdot 10^{5}$ | $W/m^3$ |
| Superficial gas velocity | 0.4 - 1.1 | m/s |
| Minimum fluidization velocity | 0.2455 | m/s |
| Coefficient of restitution | 0.60 | - |
| Wall restitution coefficient | 0.97 | - |

Initial temperature conditions were determined using the CSTR assumption as described in section 4 for simulations with different superficial gas velocities. Initial temperature condition for these simulation are listed in Table 15.

Table 15: Initial temperature condition varying superficial gas velocity

| **Initial temperature conditions** | | | | | | | | |
|---|---|---|---|---|---|---|---|---|
| | Case A | Case B | Case C | Case D | Case E | Case F | Case G | Case H |
| $u_g$ (m/s) | 0.4 | 0.5 | 0.6 | 0.7 | 0.8 | 0.9 | 1.0 | 1.1 |
| $T_g$ (K) | 337.32 | 335.29 | 334.05 | 332.94 | 332.37 | 331.73 | 331.19 | 330.72 |
| $T_s$ (K) | 337.63 | 335.55 | 334.34 | 333.25 | 332.68 | 332.09 | 331.59 | 331.06 |

First the effect of superficial velocity on the hydrodynamics is discussed. It is expected that an increase in superficial gas velocity will lead to an increase of bubble formation, collisions between particles and consequently a more chaotic behavior. In Figure 15 results are presented in a qualitative way, the snapshot were taken from a slice in the center of the reactor.

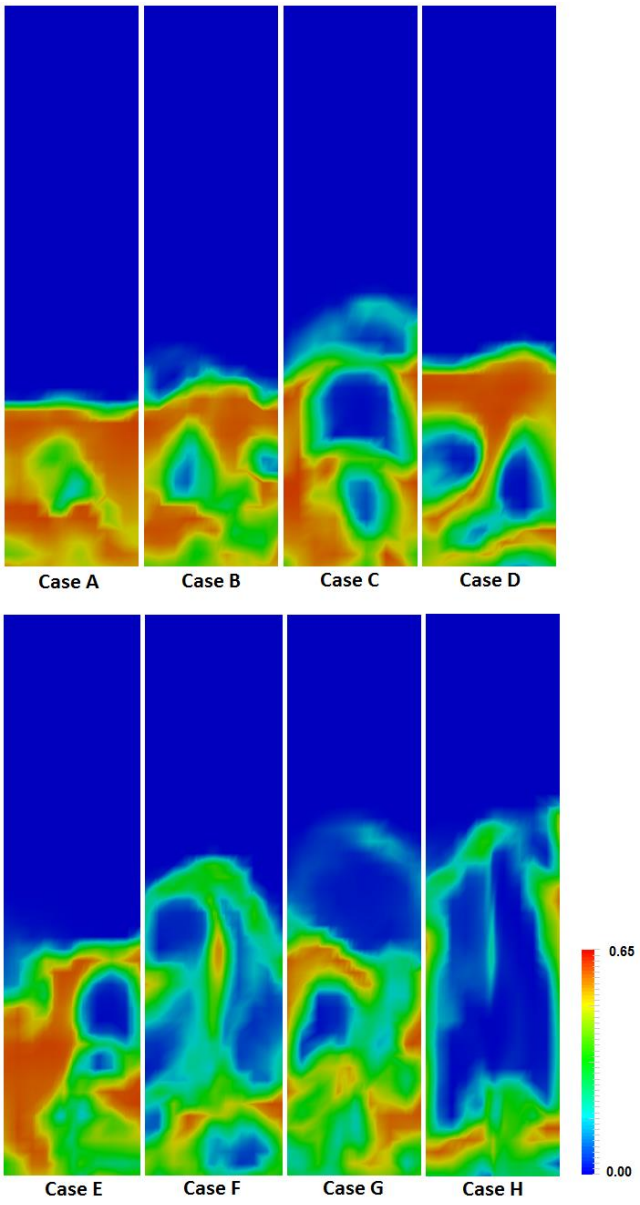


Figure 15: Snapshots of solid fraction at various superficial gas velocities.

From these snapshots it can be easily seen that a higher superficial gas velocity leads to increase in the bed height due to higher bubble formation rate.

This effect was also investigated in a quantitative manner by plotting the probability distribution function (PDF) of gas volume fraction. This PDF is calculated with equation (5.1), within this function the freeboard of the reactor is not taken into account. However, the varying cell volumes are taken into account. One should keep in mind, results that are calculated with this distribution are

dependent on the number of bins ($i$) that are used, and should be kept constant (50 in this case) for comparing of different cases. The bin width should also be kept constant when comparing results.

$$PDF_i = \frac{\sum_{k \in S_i} V_k \rho_{g,k}}{\sum_{k \notin FRB} V_k \rho_{g,k}} \begin{cases} \varepsilon_k \in \left( \varepsilon_i - \frac{\Delta\varepsilon}{2}, \varepsilon_i + \frac{\Delta\varepsilon}{2} \right] \rightarrow k \in S_i \\ FRB = freeboard \end{cases} \tag{5.1}$$

The calculated PDF's for the different cases are plotted In Figure 16. In general, three phases can be distinguished: the emulsion phase ($\varepsilon_g$<0.55), the intermediate phase ($0.55<\varepsilon_g<0.85$) and the bubble phase ($\varepsilon_g$>0.85). Two trends are visible in this graph. The first one is that with an increase in gas velocity the emulsion phase tends to get smaller. The second trend is that with increasing gas velocity the bubble phase becomes larger. This additional bubble formation leads to a better mixing and contacting of the solid phase by the gas. This will indirectly lead to a more uniform temperature in the bed.

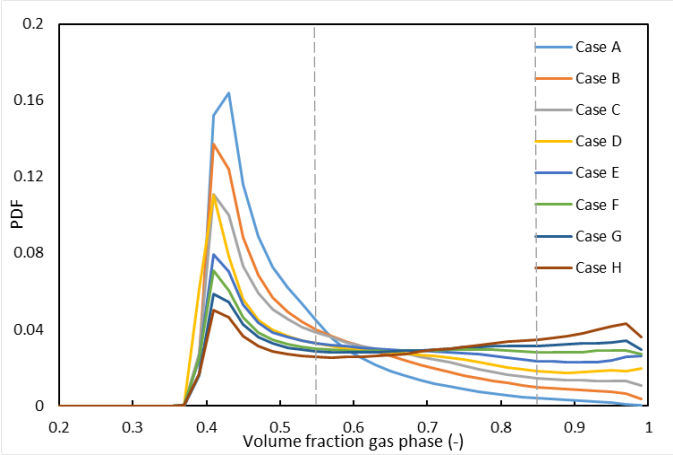


Figure 16: PDF of gas fraction for different superficial velocities

## 5.2 Effect of superficial gas velocity on heat transfer properties

As already can be overserved from the initial temperature condition, a higher superficial gas velocity will result in a lower bed temperature. This can also be seen in the average temperature plot for the gas and solid phases, respectively in Figure 17 and Figure 18. This is devoted to the fact that a higher velocity comes with a higher volumetric gas flow. Thus, more heat can be removed from the bed in this way.

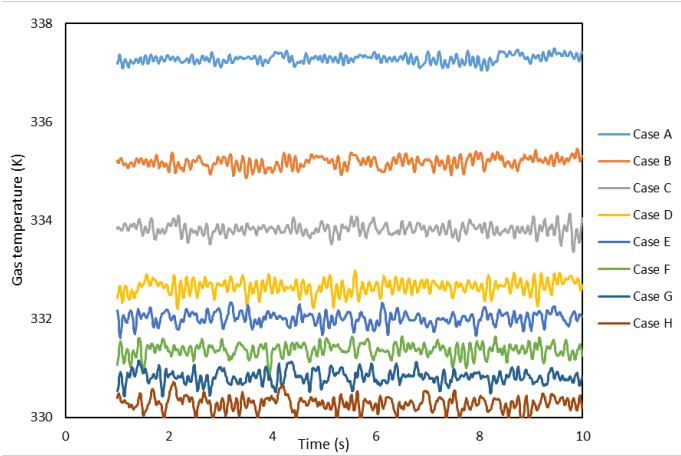


Figure 17: Average gas temperature as function of time, 6cm bed

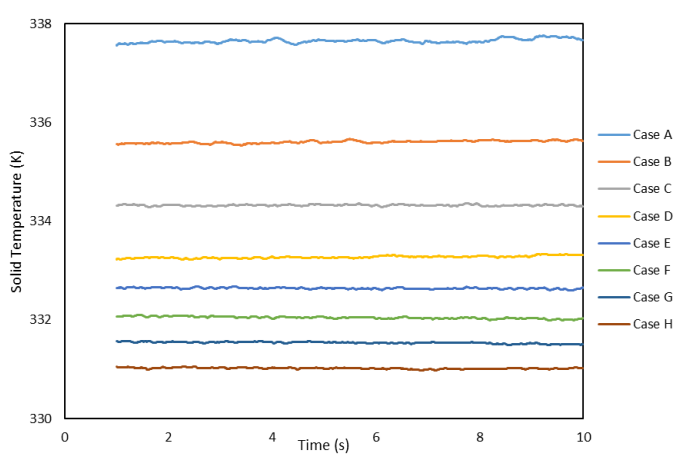


Figure 18: Average solid temperature as function of time, 6cm bed

It is more interesting to look at the temperature distributions in the bed. As [1] investigated the effect of superficial gas velocity with DEM model, it was found that a higher velocity leads to a more homogenous temperature throughout the bed. Therefore, temperature distributions have been calculated using a probability distribution function by equation (5.2). For the calculation of these PDF's the 324 to 340K range is divided in 60 equidistance bins.

$$PDF_i = \frac{\sum_{k \in S_i} V_k \varepsilon_{s,k}}{\sum_{k \notin FRB} V_k \varepsilon_{s,k}} \begin{cases} T_k \in \left( T_i - \frac{\Delta T}{2}, T_i + \frac{\Delta T}{2} \right] \rightarrow k \in S_i \\ FRB = freeboard \end{cases} \tag{5.2}$$

Probability density functions of gas and solid temperature are given in Figure 19 and Figure 20.

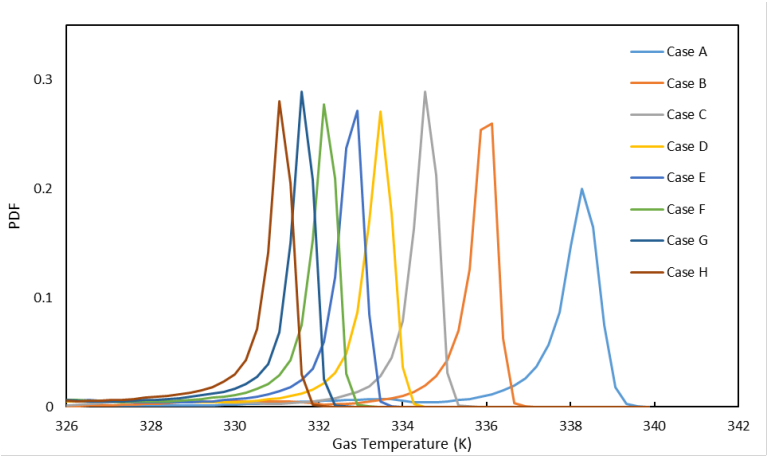


Figure 19: PDF gas temperature, number of bins = 50

From both PDF graphs it can be seen that the higher superficial gas velocity has influence on the distribution of the temperature. The width of the temperature distribution decreases with an increase of gas velocity. This trend is visible for the solid and the gas temperature. As described earlier, at higher velocities the gas is in better contact with the solid phase. As the interaction between both phases becomes more chaotic with gas velocity, the (hot) solid phase can be in contact with the (cold/fresh) gas more easily. This effect will result in a more uniform temperature distribution for both phases.

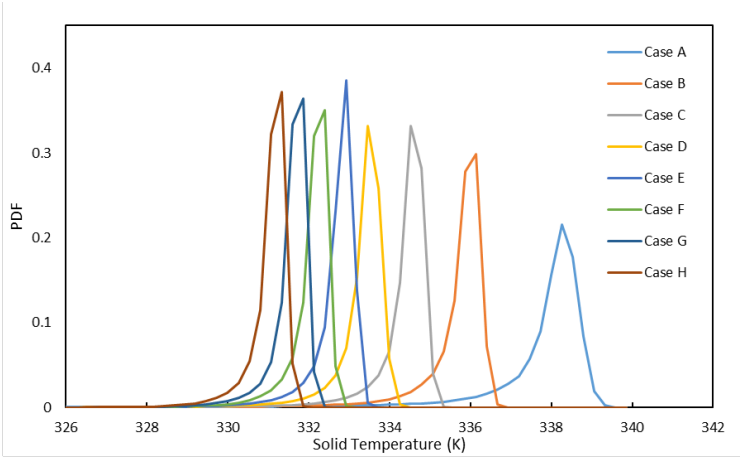


Figure 20: PDF solid temperature, 6cm bed, number of bins = 50

Another way for presenting the PDF results is in the form of a cumulative distribution function (CDF), equation (5.3). Both CDF's for gas and solid phase are presented in Figure 21 and Figure 22.

$$CDF_i = \frac{\sum_{k \in S_i} V_k \varepsilon_{s,k}}{\sum_{k \notin FRB} V_k \varepsilon_{s,k}} \begin{cases} T_k \leq T_i \rightarrow k \in S_i \\ FRB = freeboard \end{cases} \tag{5.3}$$

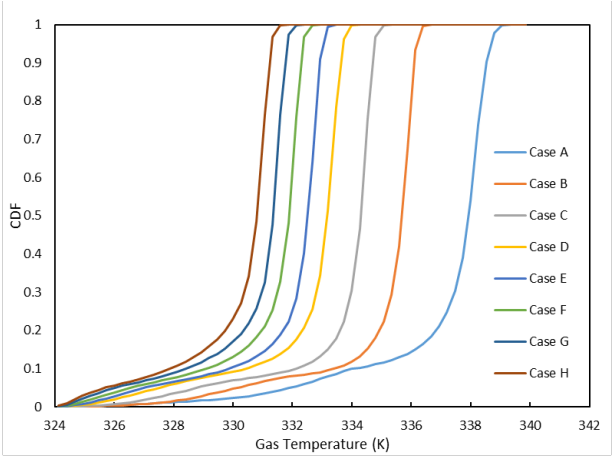


Figure 21: Gas temperature, cumulative PDF

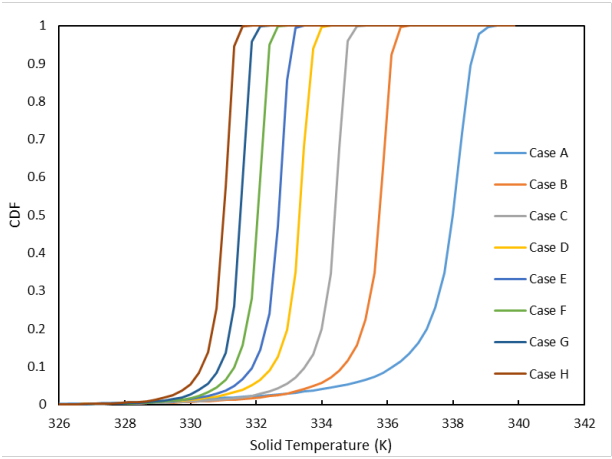


Figure 22: Solid temperature, cumulative pdf

By comparing the gas and solid CDF's, it can be observed that the distribution of the gas temperature starts at a lower temperature compared to the solid temperature. Gas is fed at 324K, therefore a tail has been observed in the gas CDF (Figure 21).

The narrower temperature distribution at higher superficial gas velocity is even more visible via CDF graphs. The steepness of the CDF indicates the width of the distribution. Higher superficial velocities result in steeper CDF graphs, and therefore narrower and more uniform temperature distribution.

This phenomenon was also seen via standard deviation. Standard deviation was calculated by equation (5.4). Standard deviation for the solid phase temperature at various superficial gas velocities is plotted in Figure 23.

$$\sigma_T = \sqrt{\sum_{i=1}^{N_{bins}} \left[ \left( T_i - \overline{T} \right)^2 \cdot PDF_{T_i} \right]} \tag{5.4}$$

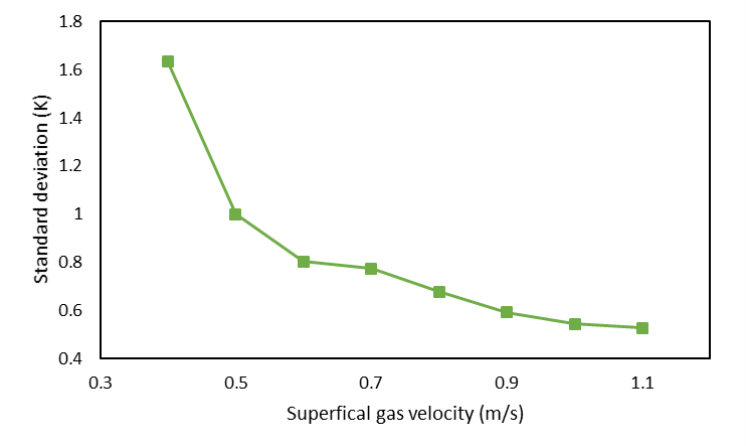


Figure 23: Standard deviation of solid temperature as a function of superficial gas velocity

Studying the influence of superficial gas velocity also includes a comparison between the maximum monitored temperatures in the bed during the whole simulation time. The maximum gas and solid temperature for simulations at different velocities are listed in Table 16. A decreasing trend is visible with increasing superficial velocity. It is also observed that the maximum gas and solid temperatures are very close to the average bed temperature.

Table 16: Maximum temperatures with varying gas velocity

| $u_g$ (m/s) | Max. $T_g$ (K) | Max. $T_s$ (K) |
|---|---|---|
| 0.4 | 340.4881 | 340.6746 |
| 0.5 | 337.5139 | 337.7721 |
| 0.6 | 336.0343 | 336.0573 |
| 0.7 | 334.8638 | 335.5007 |
| 0.8 | 334.5074 | 335.2674 |
| 0.9 | 333.6944 | 334.8530 |
| 1.0 | 333.3114 | 333.8698 |
| 1.1 | 333.0681 | 334.2290 |

Furthermore, averaged Nusselt numbers were calculated for all the performed simulations. For this purpose, we used the empirical Gunn correlation (2.13). The averaged Nusselt number was calculated by considering the importance of solid fraction and cell volume (equation(5.5)). The Nusselt number found via this equation is subsequently averaged over time.

$$\langle Nu \rangle = \frac{\sum_{i=N_{cell}} \varepsilon_{s,i} V_i \cdot Nu_i}{\sum_{i=N_{cell}} \varepsilon_{s,i} V_i} \tag{5.5}$$

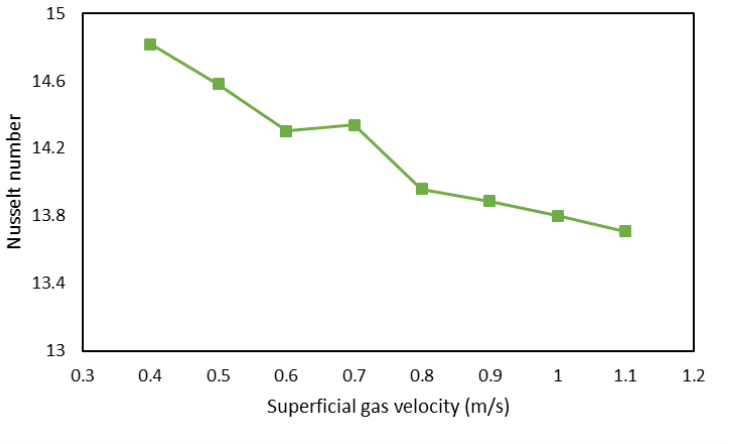


Figure 24: Spatial and time average Nusselt number as function of gas velocity.

As can be seen in Figure 24, Nusselt number slightly decreased with gas velocity in the performed simulations. This was also observed by [1]. For this reason, better heat transfer between the solid and gas phases can be excluded as a reason for the more homogenous temperature distribution at higher superficial gas velocities.

Concluding, the results that were obtained with the aid of a two fluid model are in line with the results that were obtained by DEM simulation [1]. Similar trends are observed. The two fluid model is therefore a reliable platform for simulating small lab scale fluidized bed reactors.

## 5.3 Effect of bed size

In this section, the simulations were performed for beds with 12 cm diameter and its results were compared to the case that was discussed in previous section. For all the simulations, the aspect ratio was kept constant and equal to one. All the simulation conditions for these simulations are presented in Table 17.

Table 17: Overview simulations effect of bed size

| **Simulation conditions** | | |
|---|---|---|
| Bed diameter | 0.12 | m |
| Bed height | 0.12 | m |
| Aspect ratio | 1 | - |
| Void fraction | 0.60 | - |
| Particle diameter | $9.875 \cdot 10^{-4}$ | m |
| Inlet gas temperature | 324 | K |
| Pressure | 101325 | Pa |
| Heat production | $6.7 \cdot 10^{5}$ | $W/m^3$ |
| Superficial gas velocity | 0.4-1.1 | m/s |
| Minimum fluidization velocity | 0.2455 | m/s |
| Coefficient of restitution | 0.60 | - |
| Wall coefficient of restitution | 0.97 | - |

The initial temperature conditions were determined with the aid of CSTR assumption as it is described in the previous chapter. These conditions are listed in Table 18. As can be deduced from these data, the steady state temperature in the larger beds is higher. This can be explained as the volume of the bed increases with the power of three, and the gas flow and particles' surface only increases with the power of two. As a result, more heat is produced and less cooling is applied. For this reason, a higher steady state temperature was found. For the same reason, the differences in temperature between the individual cases is larger.

Table 18: Inlet temperature condition 0.12m bed simulation with varying superficial gas velocity

| **Initial temperature conditions** | | | | | | | | |
|---|---|---|---|---|---|---|---|---|
| | Case A | Case B | Case C | Case D | Case E | Case F | Case G | Case H |
| $u_g$ (m/s) | 0.40 | 0.50 | 0.60 | 0.70 | 0.80 | 0.90 | 1.00 | 1.10 |
| $T_g$ (K) | 355.11 | 350.06 | 346.88 | 344.46 | 342.39 | 340.97 | 339.62 | 337.72 |
| $T_s$ (K) | 355.33 | 350.30 | 347.25 | 344.83 | 342.79 | 341.34 | 340.07 | 338.06 |

For studying the hydrodynamics, the gas fraction PDF were calculated and plotted in Figure 25. To do so, the gas fraction [0, 1] domain was divided in 50 equidistant bins. It was found that bubble phase becomes bigger and emulsion phase shrinks with gas velocity. This observation was similar to the outcomes of simulations for the bed with 6 cm diameter. On the other hand,one could see that the bubble region for the 12cm beds is much larger than to the bubble region for the 6cm beds. Also the increase in the intermediate phase for the 6cm beds is much smaller than in the 12cm beds. Apperently, the large bed diameter enhances bubble formation.

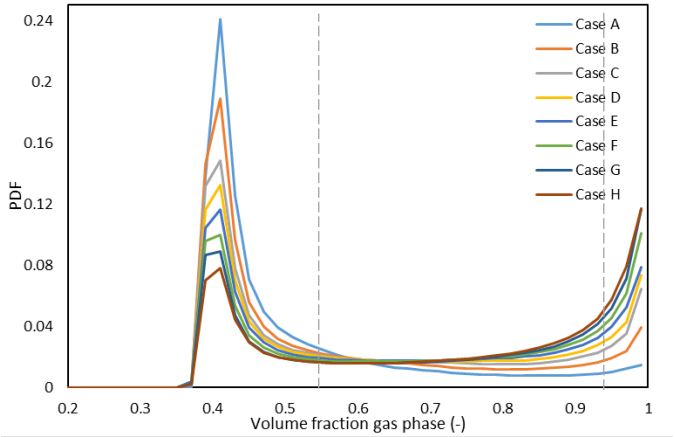


Figure 25: Void fraction 12cm bed simulation with various superficial gas velocities

Besides the hydrodynamics, the thermal behavior of the bed was also studied. First the average temperatures are discussed, as can be seen in Figure 26 and Figure 27. As noted, for a higher superficial gas velocity the bed has a lower steady state operating temperature. This is due to the fact that higher superficial gas velocity causes more cooling as the temperature of the incoming gas is lower. The solid phase temperature had less fluctuations compared to the gas phase temperature. This is explained by the much lower density and consequently heat capacity of the gas. The average gas temperature tends to fluctuate more at higher superficial velocity than it does at lower velocity, this might be a result of the larger bubble phase. Formation and eruption of bubbles cause fluctuations in the bed dynamics. Therefore, higher bubble formation rate means higher fluctuations in the bed dynamics and consequently gas temperature.

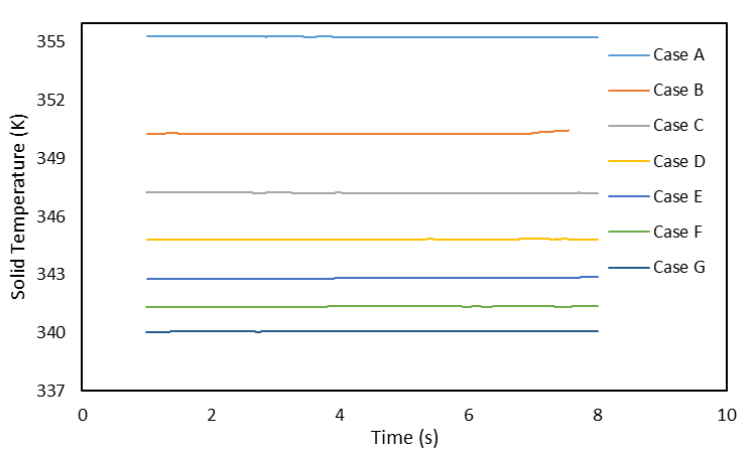


Figure 26: Time functionality of average solid temperature at various superficial gas velocity

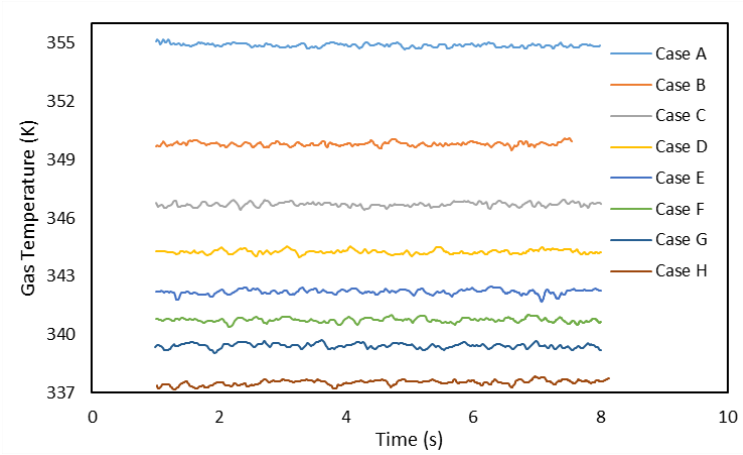


Figure 27: Time functionality of average gas temperature at various gas velocities

Temperature distribution of the different cases were calculated by (5.2) and the results are plotted for solid and gas phases in Figure 28 and Figure 29 respectively. The binwidth that was used was equal to the binwidth used for the 6cm cases, as temperature distributions are broader in this cases, 135 equidistant bins in the range of 324-360K have been used in the calculation of this PDF.

The lower averaged temperatures are also visible in these graphs. It was also observed that with an increase in superficial gas velocity the distritbution of the temperature becomes smaller. This trend is seen in the solid and the gas phase. For the smaller bed, this trend was also visible.

Differences between the 6 cm and 12 cm bed can be found in the less overlap of the temperature distribution in the 12 cm case. The difference between the average temperatures for the individual cases is larger in the 12 cm bed than its corresponding values in the 6 cm beds. As the average temperatures are higher, the driving force (difference in solid and gas temperature) is bigger. More

thermal energy is exchange. The reason the that average temperature is higher is that the amount of solid is increased by a power three, but the cooling area is only increased by a power two.

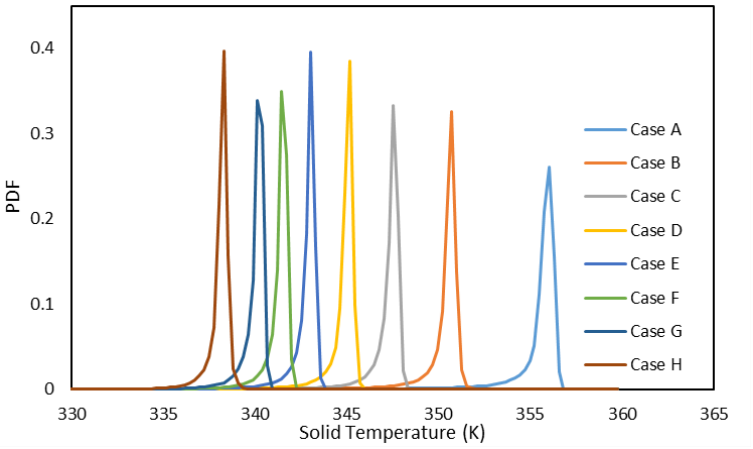


Figure 28: PDF solid temperature for different superficial gas velocities

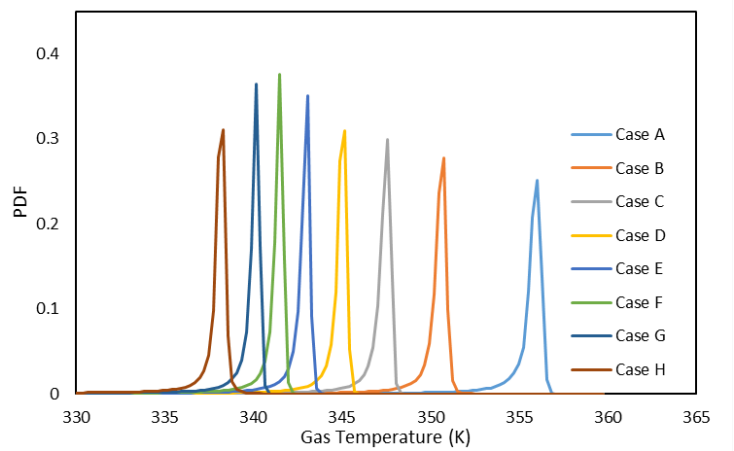


Figure 29: PDF gas temperature for different superficial gas velocities

From these PDF function the standard deviation can be deduced according to (5.4). Standard deviations were calculated and plotted in Figure 30 demonstrates the solid temperature standard deviation. The standard deviation for the 6cm bed varies between 1.6 and 0.6 K for the extreme cases. On the other hand, this parameter varies between 2.9 and 0.9 K for cases A and H in 12cm beds. An increase in bed size will therefore result in a less uniform temperature distribution in the bed.

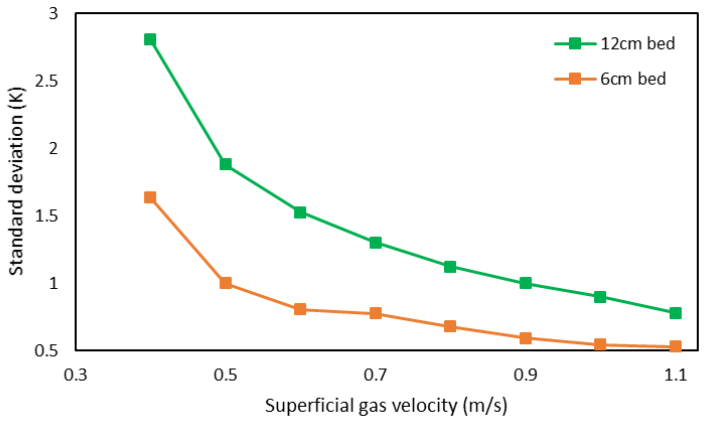


Figure 30: Comparison between solid temperature standard deviation in 6cm beds and 12cm beds at different superficial gas velocities

The average Nusselt number was also calculated for 12cm beds and the final results at different superficial gas velocities were compared with Nusselt number for 6cm beds. This comparison is presented in Figure 31. A slight decrease is observed with an increase in superficial velocity. This trend was also observed in the 6cm bed simulations. As can be seen in Figure 31 similar trend was observed for the Nusselt number calculated for the 6cm bed. A lower superficial velocities the Nusselt number matches quiet well, at higher velocities there is some deviation visible.

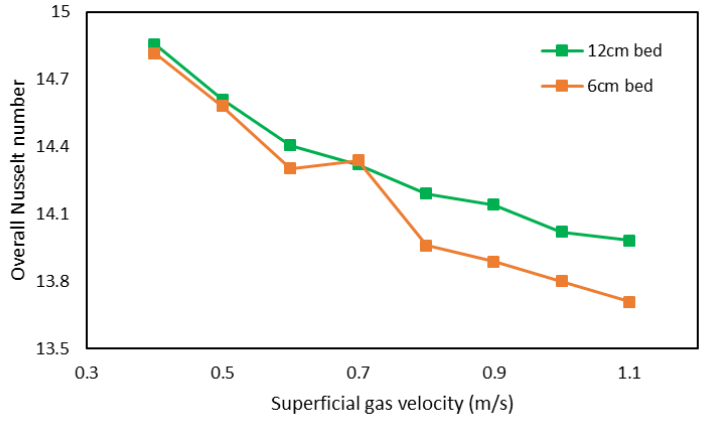


Figure 31: Comparison between overall Nusselt number in 6cm beds and 12cm beds at different superficial gas velocities

From this it can be concluded the more uniform temperature distribution at relatively high gas velocities in the bed is not a consequence of better heat transfer coefficient; but mainly to the more chaotic and intense mixing of the solid phase. This behavior was also observed during the 6cm bed simulation.

## 5.4 Effect of particle size

In this work the effect of particle size was also investigated and its results are presented in this section. In continuous operations, particle are growing in the bed. For this reason, there are always particle size distributions in an operating bed. As for the two fluid model particles are modelled as a fluid, it is not possible to implement particle size distribution within the existing code [30]. Therefore, four different simulations with different constant particle diameter were performed and their results were compared with each other. In these cases, all parameters are similar to each other except particle diameter. In this way, only the effect of particle size on solid temperature distribution and bed thermal behavior is investigated.

It is assumed the volumetric heat production, per amount of solid phase, is constant with varying particle diameter. In other words, there was not made any distinction in activeness of particles with different size. The considered cases are listed in Table 19. As stated in chapter 3, the grid cell size is chosen to be dependent on the particle diameter, different grids have been used as bed size is constant for all cases.

Table 19: Overview simulation for investigating the effect of particle size

| **Simulation conditions** | | |
|---|---|---|
| Bed diameter | 0.6 | m |
| Bed height | 0.6 | m |
| Aspect ratio | 1 | - |
| Void fraction | 0.60 | - |
| Particle diameter | $9.875 \cdot 10^{-4}$ | m |
| Inlet gas temperature | 324 | K |
| Pressure | 506625 | Pa |
| Heat production | $6.7 \cdot 10^{5}$ | $W/m^3$ |
| Superficial gas velocity | 0.51 | m/s |
| Coefficient of restitution | 0.60 | - |
| Wall coefficient of restitution | 0.97 | - |

The initial temperature conditions for the tested cases with respect to particle diameter are given in Table 20. As the minimum fluidization is function of particle diameter, different minimum fluidization velocities for the cases are given.

Table 20: Overview of different simulation cases with different particle size

| **Effect of particle diameter** | | | |
|---|---|---|---|
| Case A | Case B | Case C | Case D |
| $d_p = 4.937 \cdot 10^{-4}(m)$ | $d_p = 9.875 \cdot 10^{-4}(m)$ | $d_p = 1.234 \cdot 10^{-3}(m)$ | $d_p = 1.481 \cdot 10^{-3}(m)$ |
| $T_{s,0} = 327.35(K)$ | $T_{s,0} = 327.19(\mathrm{K})$ | $T_{s,0} = 327.13(\mathrm{K})$ | $T_{s,0} = 327.11(K)$ |
| $T_{g,0} = 327.13(K)$ | $T_{g,0} = 326.83(K)$ | $T_{g,0} = 326.76(K)$ | $T_{g,0} = 326.75(K)$ |
| $u_{mf} = 0.057(m/s)$ | $u_{mf} = 0.108(m/s)$ | $u_{mf} = 0.127(m/s)$ | $u_{mf} = 0.142(m/s)$ |

Because all the simulations were performed the same superficial gas velocity, it is trivial to have more bubble formation in the beds with smaller particles. Again a probability distribution function (PDF) was calculated by equation (5.2). This PDF was plotted in Figure 32. It is observed, the bubble phase is more present in case A compared to the cases B, C and D.

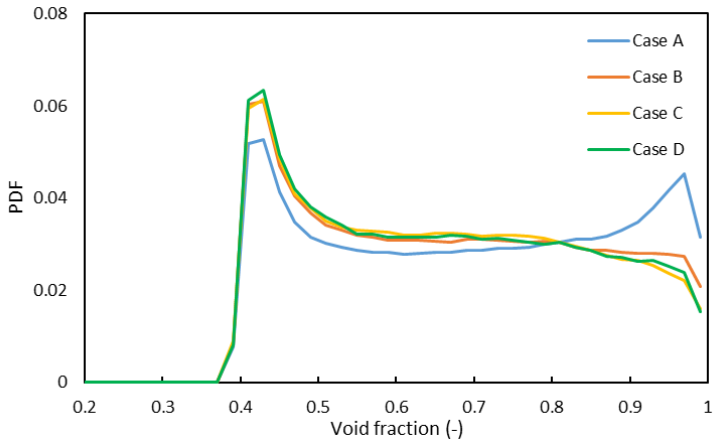


Figure 32: Effect of particle diameter on void fraction PDF

As the Geldart classification [23] for all cases were checked, it was found the smallest particles (Case A) are in the Geldart B group and the particles in the other cases behave like Geldart D. This might be the reason for the different void fraction distribution.

As can be seen in Figure 33 and Figure 34 solid and gas temperature for the simulations with different particles sizes are quite close to each other. Especially for case C and D.

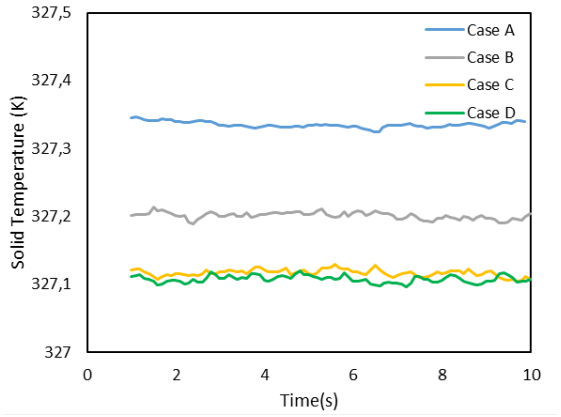


Figure 33: Average solid temperature for simulations with different particle diameters

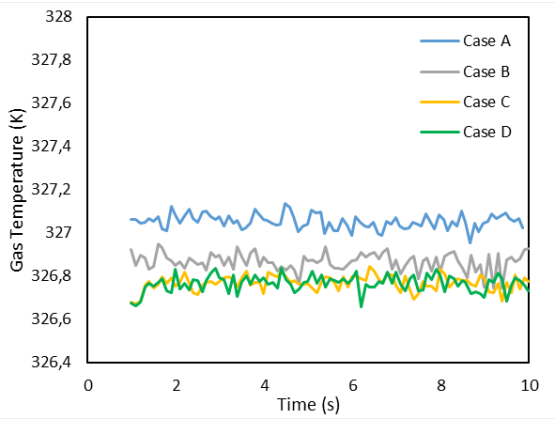


Figure 34: Average gas temperature for simulations with different particle diameters

Also for these analysis a PDF for solid and gas temperature was calculated, with the use of equation (5.2). The final results are plotted in Figure 35 and Figure 36. The difference between the widths and heights of the PDF peaks were not very large. Also the difference in standard deviation was quite small. The values of the standard deviation is reported in Table 21.

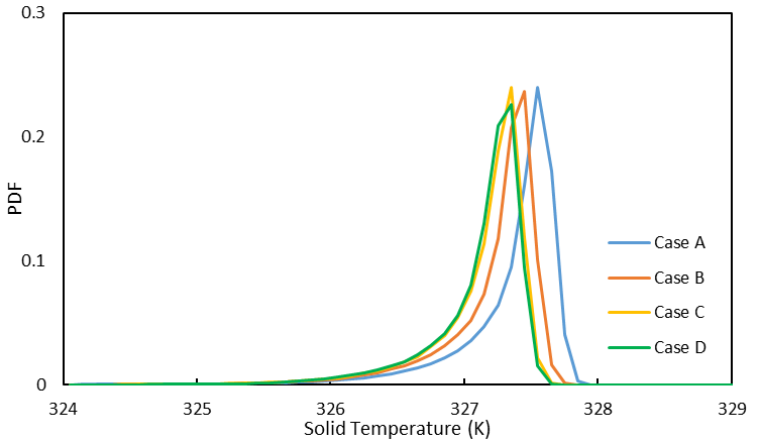


Figure 35: Effect of particle diameter on solid temperature PDF

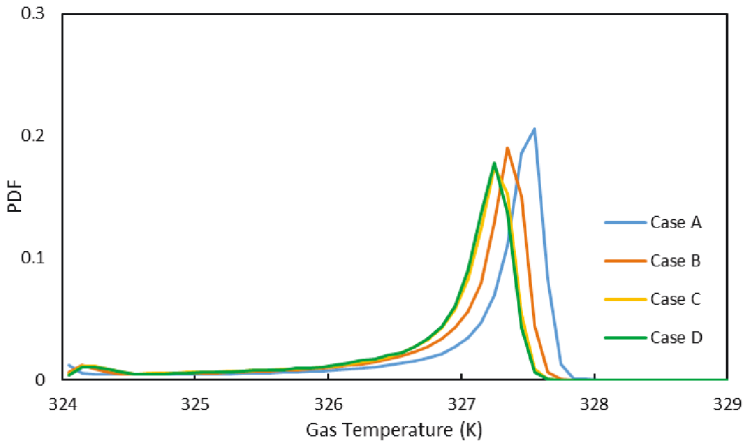


Figure 36: Effect of particle diameter on gas temperature PDF

Table 21: Standard deviation of solid temperature for simulations with different particle sizes.

| | **Standard deviation (K)** |
|---|---|
| Case A | 0.4314 |
| Case B | 0.3996 |
| Case C | 0.3976 |
| Case D | 0.3808 |

Also the heat transfer coefficient for the different cases were calculated, this was done with the empirical Gunn correlation (2.13), this number was averaged via equation (5.5). An increasing trend in Nusselt number is visible with an increase in particle diameter. This trend was also observed by [1] . For the particles in this system, it holds that the first term in de Nusselt correlation (2.13) is dominant, and is mainly determined by $\mathrm{Re}_p$ , it is therefore expected that systems with smaller particles have lower Nusselt numbers.

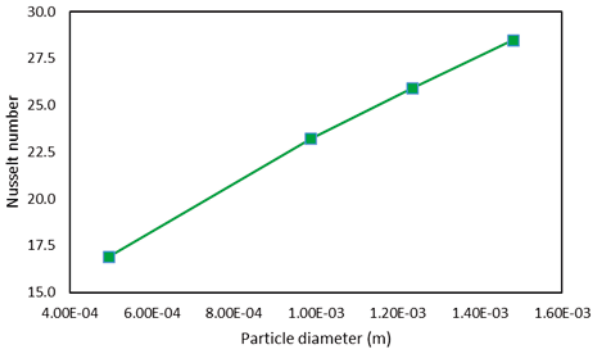


Figure 37: Average Nusselt number for varying particle sizes

# 6. Solid mixing in fluidized beds

The introduction of tracer particles opens a possibility to find out the mixing rate of solids with TFM. Fluidized bed are well known for their good mixing properties and this characteristic leads to good heat transfer properties. As it is stated in previous chapter faster solid mixing (circulation) leads to narrower solid temperature distribution. Mixing properties are difficult to characterize in experimental setups and quantifying of this parameter with modeling can give a better insight on this phenomena within chemical reactors. These analysis can also help us to have a clearer view on the mixing pattern of fresh feed in the reactor.

Earlier research to this subject is done by [6], however, complications were encountered during simulation. With evolving time, particles did not follow the solid phase anymore. In other word, the continuity equation was not satisfied by tracers. Thus a new method is presented in this work. This method does not have this deficiency and can be easily implemented into TFM. After introducing the basic principles of this technique, its verification is presented and discussed. Some sensitivity analysis were also performed and their results are also presented in this chapter. Then, the effect of restitution coefficient on the mixing rate of particles are discussed. These results are extremely helpful as we know that particles restitution coefficient may change with some operating conditions like temperature. Besides that, the effect of superficial gas velocity on the solid mixing rate was also explored. It should be noted that this methodology has not been used by any other researcher and it can be applied in other chemical and physical processes that contain powders.

## 6.1 Methodology and algorithm

The tracer particles that were used in this project do not have physical properties and do not interact with each other. Furthermore the tracer particles do not have a diameter and do not occupy volume in the fluidized bed. The method used for implementation of tracer particles consists of two parts, first the initialization of tracer particles and then modeling of the tracers' movement.

For the initialization of the tracer particles two methods were used. The first method (referred as Method 1) use a constant number of tracers. In this method a weight-factor (or probability) was devoted to each computational cell based on the cell volume and the solid fraction in the cell. The interval of zero to 1 were divided into subintervals based on weight factor, an example is given in Figure 38. In this example, cell i=2 has a larger solid content or a larger volume compare to cell i=1. Therefore a larger interval for this cell is devoted to this cell. If all cells have an interval with a certain width, these intervals are normalized (sum of all intervals should be equal to 1). Subsequently tracer

particles are distributed over these intervals randomly by using a random number between 0 and 1 for each tracer particle. In this way cells with a larger volume and higher solid fraction have the tendency to store more tracer particles due to their higher probability/larger interval. The position of every tracer particle in each cell is determined randomly, for all the coordinates (radial, azimuthal and axial) a random number is used.

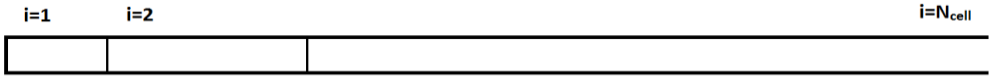


Figure 38: Example intervals of weight factor for computational cells. In this example, cell i=2 has a larger solid content compare to cell i=1. Therefore a larger interval is devoted to this cell.

The second method (referred as Method 2) that used for initialization is also based on the solid fraction and the volume of the cell. First all the cell volumes times the solid fraction are summed up and divided by the number of tracers ($T_{fraction}$) (6.1). Subsequently for each computational cell, the number of tracers is calculated by equation (6.2). This number of tracer is rounded to the nearest integer. In practice, this means the sum of all elements of this $N_{i,\mathrm{j},\mathrm{k}}$ can be different from the numbers of that was set for them initially ( $N_{tracers}$ ).

$$T_{fraction} = \frac{\sum_{i=0}^{nx}\sum_{j=0}^{ny}\sum_{k=0}^{nz} V_{i,j,k} \cdot \varepsilon_{s,i,\mathrm{j},\mathrm{k}}}{N_{Tracers}} \tag{6.1}$$

$$N_{i,j,k} = floor\left(\frac{V_{i,j,k} \cdot \varepsilon_{s,i,\mathrm{j},\mathrm{k}}}{T_{fraction}} + 0.5\right) \tag{6.2}$$

In equation (6.1) $V_{i,j,k}$ is the cell volume and $\varepsilon_{s_{i,j,k}}$ is the corresponding solid fraction in that cell. $T_{fraction}$ is volume times solid fraction that should be proportional to the number of tracer particles at that cell. In this method, the sub-grid position of a tracer particle is determined by three random numbers too. Differences between both methods are presented in the next section.

After initializing the tracer positions, their movement with solid flow should be found. For this purpose, the solid fluxes at the all the cell surfaces should be calculated and saved at every time step. Only 'leaving' flux was taken into account. The amount of solid that leaves a specific cell surface was compared to the total amount of solid at that computational cell. In this way we can calculate the leaving probability of tracers in all the directions. We can find the staying probability of tracers as

well. The summation of these probabilities are equal to 1. Again intervals were created by these possibility of leaving and not leaving as can be seen in Figure 39. One should keep in mind that Figure 39 is only a hypothetical example and in reality some intervals may not exist or have size of zero.

After creating probability interval, a random number between 0 and 1 should be generated for each tracer at the investigated cell. The interval which correspond to this random number indicates the leaving direction of the specific tracer particle. In one time step a particle can only move maximum one computational cell. This routine is repeated for each tracer particle in all the computational cells.

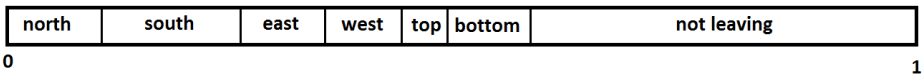


Figure 39: A hypothetical example of probability interval for determining the leaving direction of a tracer particle

## 6.2. Mixing quantification

After implementing all the necessary routines for finding the tracers' movement, we needed to quantify tracers mixing and verify the implementations. The quantification procedure is described in this section and the verification parts are presented in the following sections.

The process of mixing can be quantified by a parameter so called mixing index. The mixing index is 0 in a completely de-mixed state and it is equal to 1in a totally mixed state. In this work the nearest neighbor distance method is used [31] for calculating the mixing index (6.3). This mixing have better characteristics compared to other mixing indices. So, all the analysis in this work were done only with the aid of this definition.

$$M = \frac{\sum_{i=0}^{N} r_{ij}}{\sum_{i=0}^{N} r_{ik}} \tag{6.3}$$

Where $M$ is the mixing index, $r_{ij}$ in this equation is the distance between particle $i$ and its initially nearest neighbor particle $j$. $r_{ik}$ is the distance between particle $i$ and a random particle $k$.

## 6.3 Mixing sensitivity to the number of tracers

To investigate in which extent the results are sensitive to the choice of number of tracer particles, several simulations were performed with varying this parameter. During these simulations heat transfer was not taken into account. Besides the earlier mentioned mixing index another parameter is used to compare these simulations. This parameter is called 'continuity satisfaction parameter (CSP)', given in (6.4).

$$CSP = 1 - \frac{\sum_{i=0}^{N_{cells}} \left| (N_{n,i} - \varepsilon_{n,i}) \right|}{2} \tag{6.4}$$

In this equation $N_n$ and $\varepsilon_n$ are the normalized number of tracer and the normalized solid content respectively, given in (6.5) and (6.6).

$$N_{n,i} = \frac{N_{T,i}}{\sum_{i=0}^{N_{cell}} N_{T,i}} \tag{6.5}$$

$$\varepsilon_{n,i} = \frac{\varepsilon_i \cdot V_{cell,i}}{\sum_{i=0}^{N_{cell}} \varepsilon_i \cdot V_{cell,i}} \tag{6.6}$$

In this equation $N_{T,i}$ is the number of tracers in this cell.

The CSP is used to correlate the movement of the tracer to the movement of the solid. If the tracer particles follow the solid movement in a perfect way, CSP will be equal to 1. If the movement of the tracer is totally different from the movement of the solid, this CSP will be close to 0.

The first simple simulations with the implementation of tracer particles were performed to investigate in which extent the results of these particles are dependent on the number of tracers that are used during simulations. The tests were done by simulating a 5cm diameter fluidized bed, within this bed heat production/transfer was not considered. Further details of these simulations are given in Table 22.

Table 22: Simulation settings and condition sensitivity to number of tracers.

| **Simulation setting** | | |
|---|---|---|
| Number cells x-direction | 5 | - |
| Cell size x-direction | 0.0050 | m |
| Number cells azimuthal direction | 16 | - |
| Cell size azimuthal direction | 0.125 | m |
| Number of cells in vertical direction | 30 | - |
| Cell size vertical direction | 0.0050 | m |
| Time step | $1 \cdot 10^{-5}$ | s |
| Simulation time | 5 | s |
| **Simulation conditions** | | |
| Particle diameter | $1.5 \cdot 10^{-3}$ | m |
| Inlet gas temperature | 300 | K |
| Initial gas temperature | 300 | K |
| Initial solid temperature | 300 | K |
| Pressure | 101325 | Pa |
| Heat production | 0 | $W/m^3$ |
| Height fixed bed | 0.05 | m |
| Porosity fixed bed | 0.6 | $m^3_{bed}/m^3_{reactor}$ |
| Superficial gas velocity | 1.8 | m/s |
| Coefficient of restitution | 0.97 | - |
| Wall coefficient of restitution | 0.97 | - |

To make an (reactor size -) independent comparison between the tested scenarios, the actual number of particles, based on the particle diameter was calculated for the aforementioned simulations. Based on this number, certain percentages of this amount were tested. Eight different cases are distinguished, listed in Table 23. The results for the CSP (6.4) are depicted in Figure 40.

Table 23: Tracer sensitivity cases

| | **Case A** | **Case B** | **Case C** | **Case D** | **Case E** | **Case F** | **Case G** | **Case H** |
|---|---|---|---|---|---|---|---|---|
| % number of tracers to number of particles | 100% | 80% | 60% | 30% | 20 | 10 | 5 | 1 |

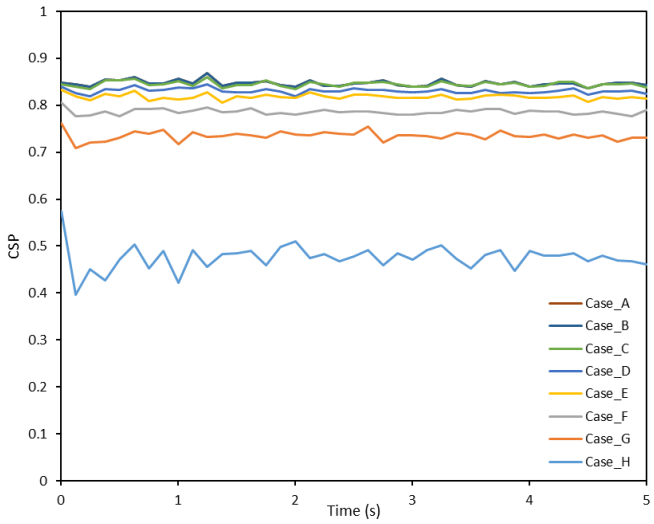


Figure 40: CSP sensitivity to the number of tracer particles

As can be deducted from Figure 40, the CSP value for most of the cases are comparable. Only for the case in which 5% of tracers were used a significant deviation is visible compared to the other cases. The reason that the maximum CSP is not 1, but 0.87, is that the introduced tracer particles can only be in 1 grid cell at a time. In reality, particles can be in multiple cells as they are at the cell border. It should also be noted that the CSP is constant during the 5 seconds of simulation, and therefore this method is able to follow the solid movement in the reactor.

From abovementioned results it was chosen to use systems with 10% (case F) of tracer particles compared to the theoretical amount of particles in the system. In the end the goal is to say something about the mixing rate within fluidized beds with varying superficial gas velocities, Figure 40: CSP sensitivity to the number of tracer particles shows this is possible to do so with 10% of tracer particles.

## 6.4 Sensitivity to initialization method

The aforementioned initialization methods were also compared with each other. For the comparison of these methods the CSP was calculated for the dump file that was generated at time step one. In Figure 41 results are plotted as function of the tracer percentage. For method 2, CSP right after initialization does not change significantly with the number of tracers. However, the CSP drops significantly just after a fraction of a second. Method 1 and method 2 did not show any advantage over each other. It was only observed that, for low amount of tracers method 2 is slightly more accurate (case H in Figure 40).

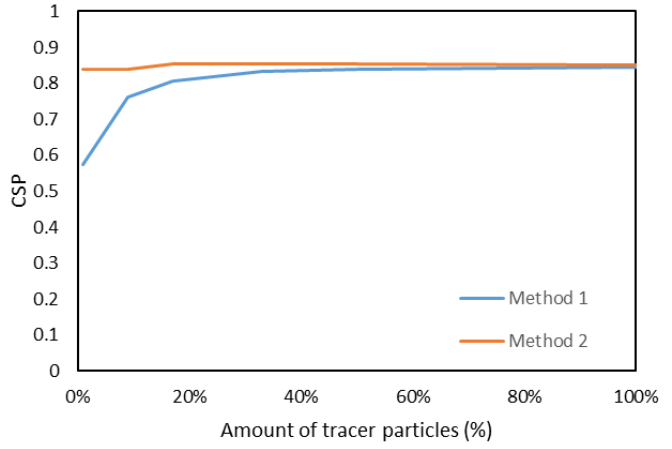


Figure 41: CSP right after initialization with using the two initialization methods as function of tracer particles percentage

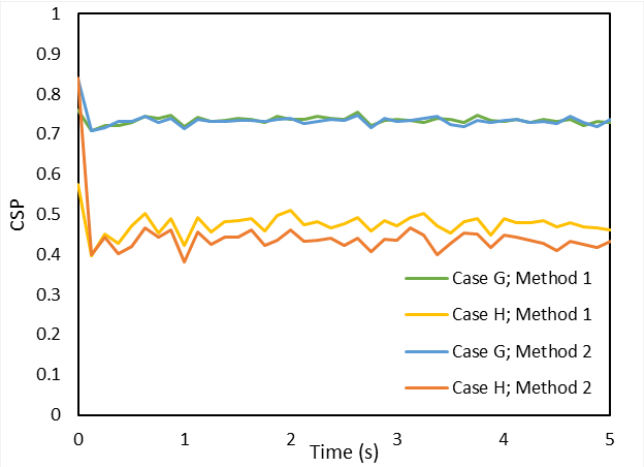


Figure 42: CSP as function of time: comparison between method 1 and method 2

It was chosen to use method 1 for the initialization for the tracer particles because of the complexity of the allocation of the memory for method 2.

## 6.4 Grid size sensitivity analysis

After finding the suitable number of tracer particles, and initialization method, the implementation of tracer particles was tested for its sensitivity to the number of grid cells. For these tests, the number of grid cells that was found during the sensitivity for the heat transfer part was taken as a reference case. For comparison of these cases the mixing index, equation (6.3) was calculated. Grid sensitivity tests were performed in three different directions. The mixing index was therefore adapted to be calculated in the horizontal and vertical directions. The simulation settings that were used during these tests are listed in Table 24. Heat transfer was not taken into account during these simulations. The difference between the tested cases is listed in Table 25. For all the cases the time-average mixing index is compared. This average mixing index is established by taking an average over five equal time intervals with the duration of 1.5s.

Table 24: Simulation condition for grid sensitivity tests

| **Simulation conditions** | | |
|---|---|---|
| Particle diameter | $9.875 \cdot 10^{-4}$ | m |
| Inlet gas temperature | 300 | K |
| Initial gas temperature | 300 | K |
| Initial solid temperature | 300 | K |
| Pressure | 101325 | Pa |
| Heat production | 0 | $W/m^3$ |
| Height fixed bed | 0.06 | m |
| Porosity fixed bed | 0.6 | $m^3_{bed}/m^3_{reactor}$ |
| Superficial gas velocity | 0.7 | m/s |
| Coefficient of restitution | 0.97 | - |

Table 25: Test cases for grid sensitivity tests

| | **Radial** | | | **Axial** | | | **Azimuthal** | | |
|---|---|---|---|---|---|---|---|---|---|
| Case | *A* | *B* | *C* | *D* | *E* | *F* | *G* | *H* | *Ref.* |
| Radial cells | 6 | 8 | 12 | | 60 | | 10 | | 10 |
| Radial cell size (m) | 0,005 | 0,00375 | 0,0025 | | 0.003 | | 0,003 | | 0,003 |
| Axial cells | | 32 | | 36 | 45 | 72 | 10 | | 60 |
| Axial cell size (m) | | 0,0625 | | 0,005 | 0,004 | 0,0025 | 0,003 | | 0,003 |
| Azimuthal cells | | 32 | | | 32 | | 16 | 40 | 32 |
| Azi. cell size (m) | | 0,0625 | | | 0,0625 | | 0,125 | 0,05 | 0,0625 |

First cases A, B, and the reference case are compared for checking the algorithm for radial grid sensitivity. The mixing index for the horizontal direction is calculated and plotted in Figure 43, the overall mixing index for these cases is plotted in

Figure 44. In both figures, a constant mixing index is observed for the cases B, C and the reference case. This indicates the calculated index is not dependent on grid size anymore. As for the heat transfer cases there was chosen to use a grid size of 0.003m in the radial direction, for the implantation of tracer particle there has also been chosen for this same grid size.

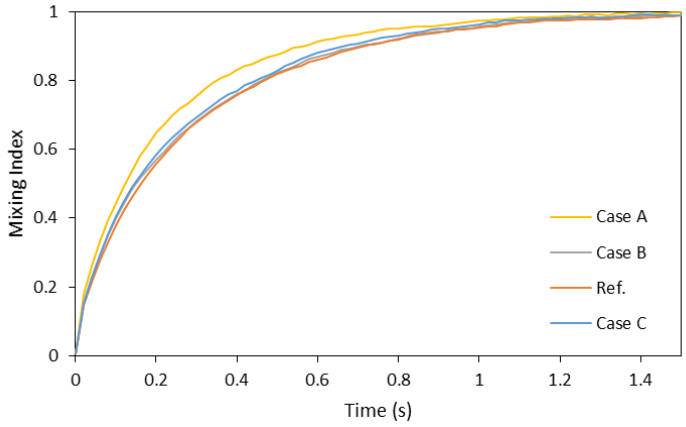


Figure 43: Horizontal mixing index, radial grid refinement

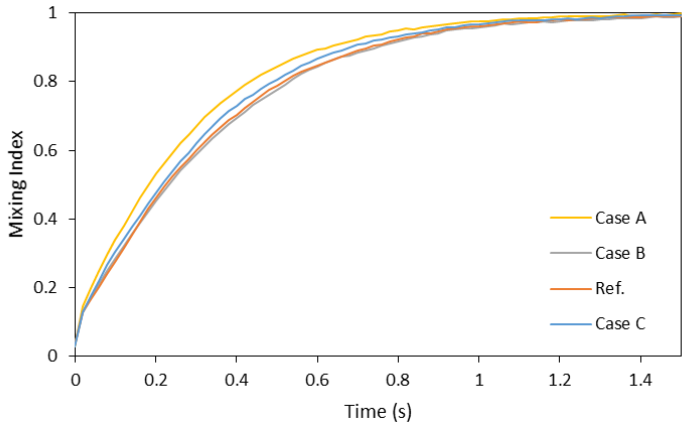


Figure 44: Overall mixing index; radial grid refinement

Secondly the cases D, E, F and the reference case are compared for checking the algorithm for axial grid sensitivity. The vertical and overall mixing indexes are calculated and plotted in Figure 45 and Figure 46 respectively. As can be seen in Figure 45, the vertical mixing index does not reach to a steady solution with a decrease in grid size (an explanation for this is given later on). For the overall mixing index (Figure 46) a steady solution is found (reference Case and Case F), clearly the mixing in horizontal direction is dominant over the vertical direction in the calculation of the overall mixing index. This can be concluded for two reasons; the mixing in vertical direction is much faster than the overall mixing (0.75s vs 1.5s).

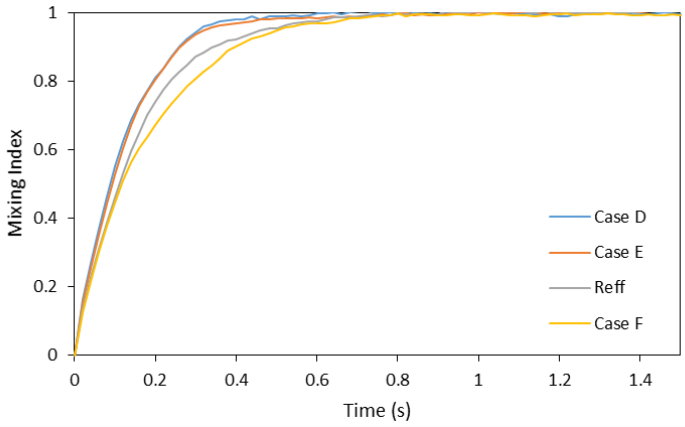


Figure 45: Vertical mixing index, axial grid refinement

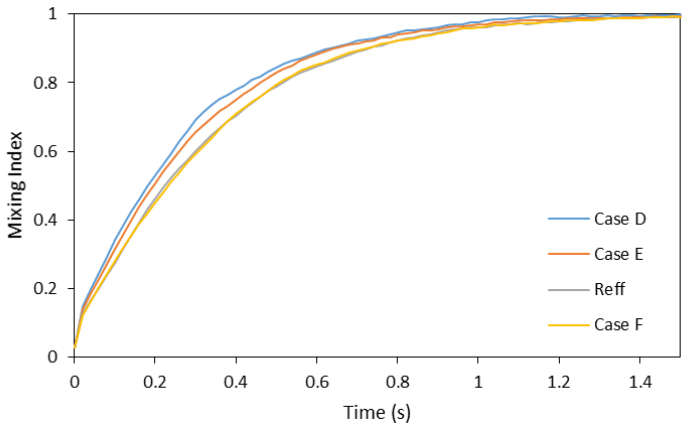


Figure 46: Overall mixing index, axial grid refinement

An explanation for the unsteady solution for the abovementioned cases in the vertical mixing index revealed a deficiency of the method for moving the particles. This drawback can be shown by a simple example. When a perfect plug flow situation is considered in which only particles are moving and the velocity is set constant to 0,5m/s, and a time step of 1 second (Figure 47). As according to the method applied, 100% of the tracer within the cell is leaving, and subsequently random positioned in the 'new' cell. When this example is done with bigger cells (Figure 48) in this case only a random 50% of the cell content is leaving. Again the tracers will be positioned randomly in the new next cell.

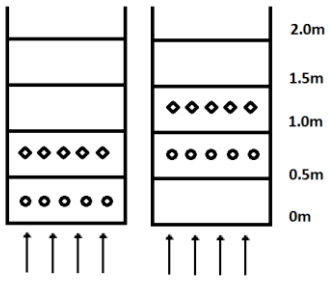


Figure 47: Mind experiment case 1, on the left initial situation and on the right after one time step

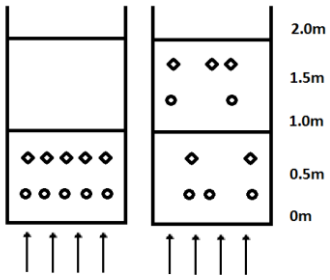


Figure 48: Mind experiment case 2, on the left the initial situation and on the right after one time step

As can be seen in these figures, two different cases are obtained for this simple case. As a plug flow was applied no mixing should occur, but in case 2 particles have been mixed after the first time step. There is also a wide region in which particles are present. In case 1, all the particles are between 0.5 and 1.5 meters. In case 2 particles can be found between 0 and 2m. Of course, the considered case is extremely exaggerated and the difference between the cases is chosen to show this phenomena. It is clearly shown some 'false diffusion'. This effect can be not excluded as a disadvantage of the applied method.

On the other hand, with an increase in the number of grid cells in the axial direction tracer particles are limited to travel larger distances within one time step. For the discussed cases the CSP (equation (6.4)) is calculated and the results are presented in Figure 49. As can be seen, with an increase in the number of grid cells in vertical direction, the CSP decreases too. So, we should have made a compromise between these two effects. Further investigations on these cases can give us a better understating and it is highly recommended.

For the simulation there has been chosen to use the grid size that was used in the reference case, 0.003m. This is in line with the settings used during the heat transfer simulations.

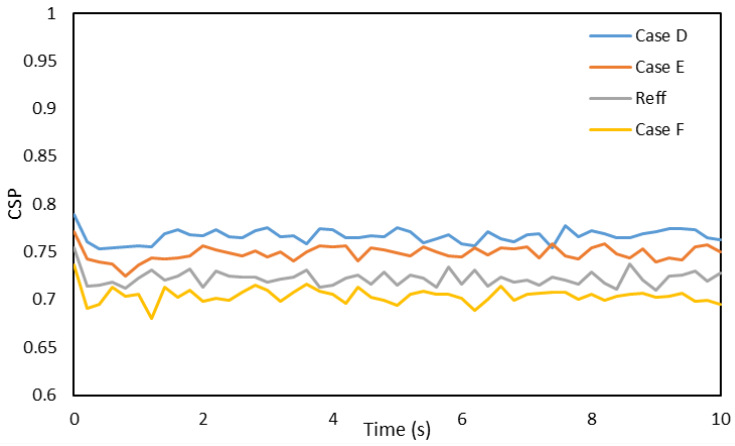


Figure 49: CSP for axial grid refinement

To complete the grid sensitivity analysis, case G, H and the reference cases are compared for investigating the sensitivity in azimuthal direction. Again the mixing index for the horizontal direction and the overall mixing index were calculated. Results are presented in Figure 50 and Figure 51. Again for this analysis it is observed that results shows grid independency if sufficient number of grids are used.

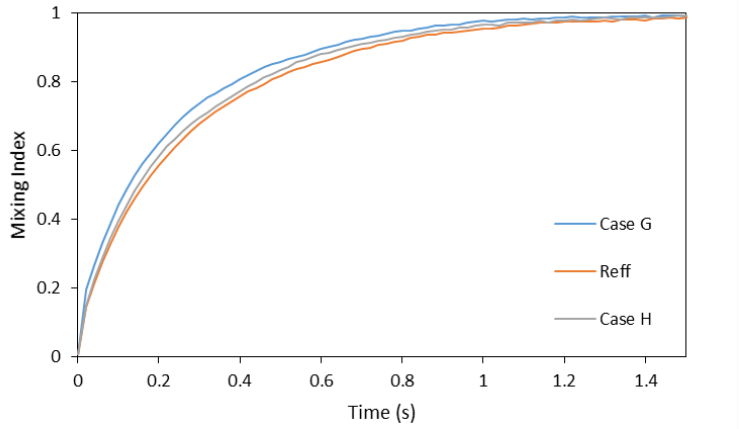


Figure 50: Horizontal mixing index; azimuthal grid refinement

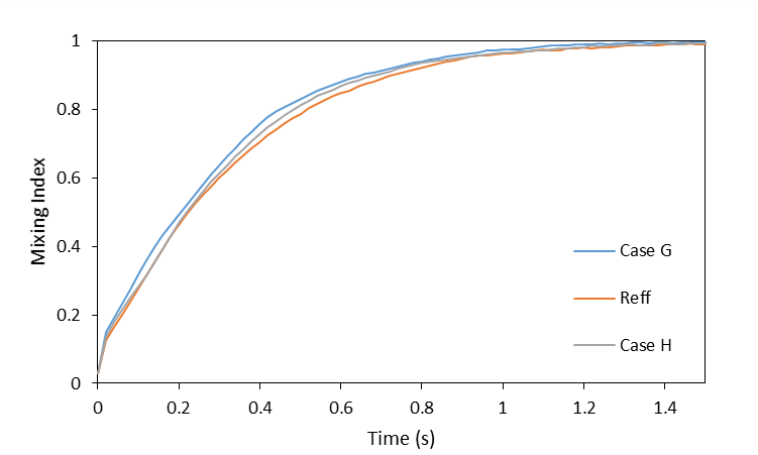


Figure 51: Overall mixing index; azimuthal grid refinement

Also for the azimuthal direction there is been chosen to use same amount of grid cells that are used in the reference case, this is in line with the grid sizes that were used during the heat transfer simulations.

## 6.5 Effect of superficial gas velocity

Within this chapter the effect of superficial on the mixing behavior is discussed. Simulation setting are listed in Table 26, an overview of the tested cases is given in Table 27. These simulations are similar to the simulations for analyzing the thermal behavior of the bed.

Table 26: simulation condition mixing simulation

| **Simulation conditions** | | |
|---|---|---|
| Bed diameter | 0.6 | m |
| Bed height | 0.6 | m |
| Aspect ratio | 1 | - |
| Void fraction | 0.60 | - |
| Particle diameter | $9.875 \cdot 10^{-4}$ | m |
| Inlet gas temperature | 324 | K |
| Pressure | 101325 | Pa |
| Heat production | $6.7 \cdot 10^{5}$ | $W/m^3$ |
| Superficial gas velocity | 0.4-1.1 | m/s |
| Minimum fluidization velocity | 0.2455 | m/s |
| Coefficient of restitution | 0.60 | - |
| Wall coefficient of restitution | 0.97 | - |

Table 27: Tested cases mixing simulations

| | Case A | Case B | Case C | Case D | Case E | Case F | Case G | Case H |
|---|---|---|---|---|---|---|---|---|
| $u_g$ (m/s) | 0.4 | 0.5 | 0.6 | 0.7 | 0.8 | 0.9 | 1.0 | 1.1 |

For comparison of the results, the mixing indices between the cases are compared, equation (6.3). As discussed in chapter 5, a higher superficial gas velocity will lead to more bubble formation and a more intense contact between the solid and the gas phase. It is therefore expected to have a faster mixing with increasing the superficial gas velocity.

First qualitative results are presented in the form of simulation snapshots of the tracer particle. To visualize the mixing, during the post processing of the result half of particles were colored red or blue. Snapshots for case B (0.5m/s), case E (0.8m/s) and case H (1.1m/s) are depicted in Figure 52, Figure 53 and Figure 54, respectively. It is observed the bed height increases with an increase in gas velocity, hence higher bubble formation.

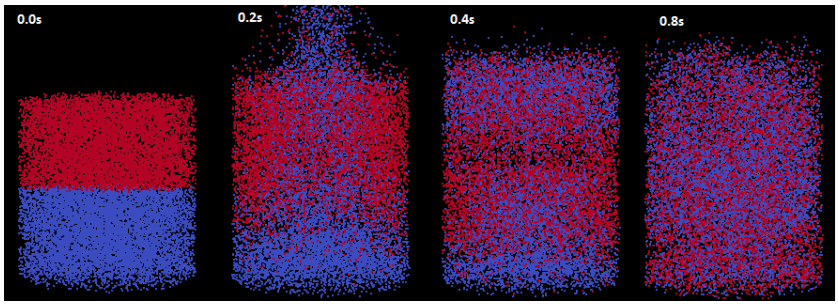


Figure 52: Snapshot of tracer particles for case B (0.5m/s) at different times

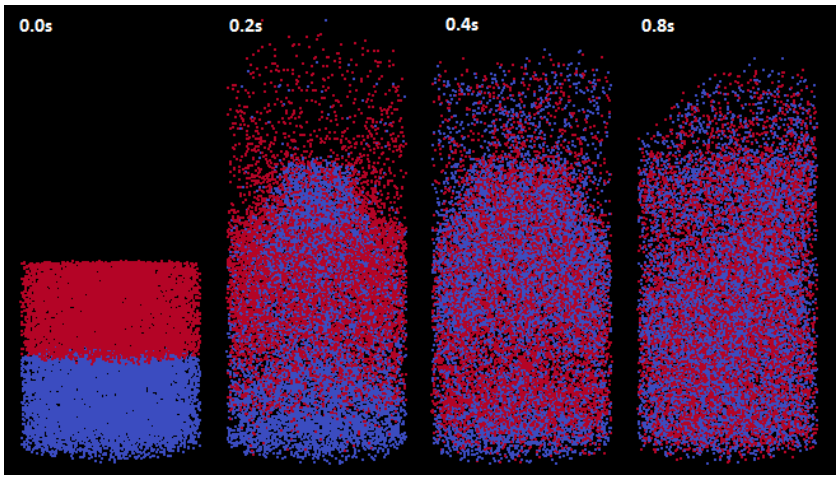


Figure 53: Snapshot of tracer particles for case E (0.8m/s) at different times

For quantitative comparison of the tested cases the mixing index was calculated. The mixing index was averaged over five equal time intervals at each simulation. These time intervals were chosen after the startup phase of the reactor, when there was no symmetry in solid distribution in the bed. Besides an overall mixing index, indexes have been calculated for horizontal and vertical direction and plotted in Figure 55. The overall mixing index presented in Figure 56.

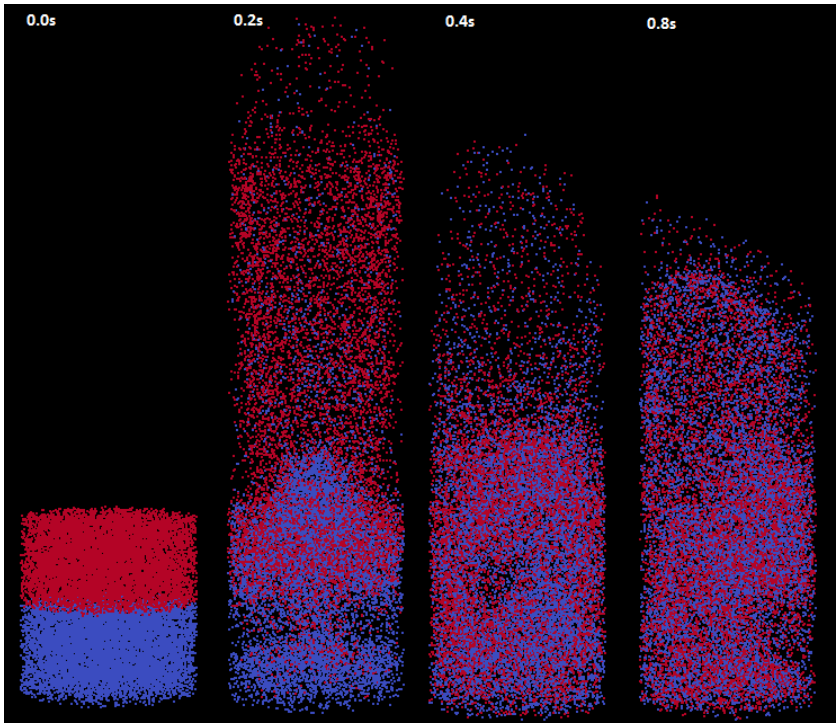


Figure 54: Snapshot tracer particles case H (1.1m/s) for different times

It was observed that at relatively high gas velocities, the mixing index reached to one faster. It was also observed that vertical mixing happens much faster than the horizontal mixing. However, an increase in gas velocity has more influence on the mixing in horizontal direction than in vertical direction. This effect on the horizontal mixing is therefore dominant in the overall mixing index.

These findings are in line with the earlier results; the more homogenous temperature distribution that was discussed in previous chapters. This more uniform distribution is the results of faster mixing; due to this faster mixing a more intense contact between gas and solid phase takes place. Hot particles can be in contact with the cold incoming gas flow more often and faster at relatively high gas velocities compared to the cases with relatively low gas velocities.

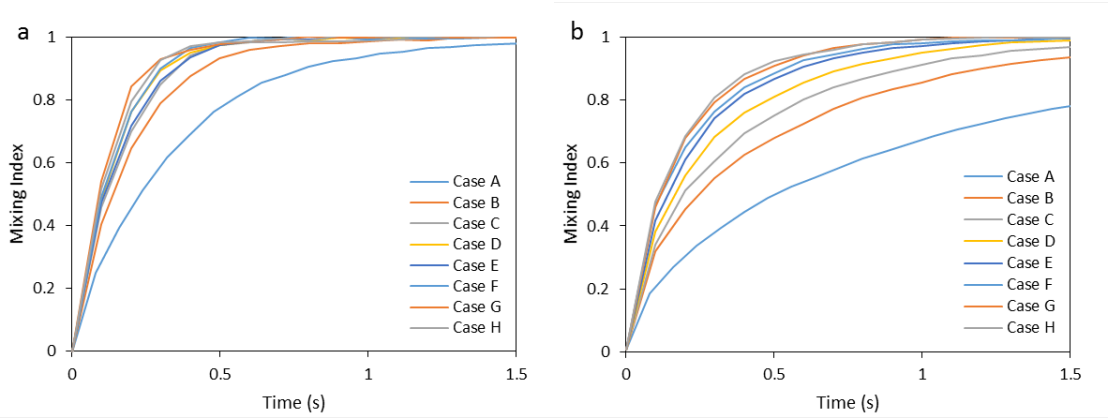


Figure 55: Effect of superficial gas velocity on the mixing index in vertical direction (Figure 55a) and in the horizontal direction (Figure 55b)

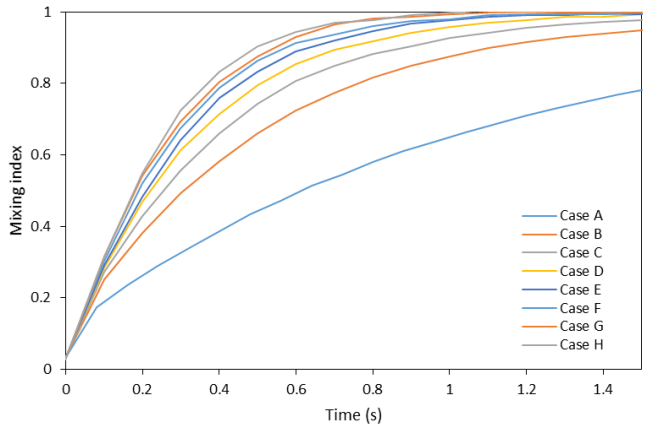


Figure 56: Effect of superficial gas velocity on the overall mixing index

To quantify the obtained results in a clearer way, an exponential function in the form of equation, (6.7) were fitted to the results. $A$ and $b$ in this function are the fitting parameters.

$$M = 1 - Ae^{-bt} \tag{6.7}$$

It should be noted that for fitting results that are plotted in Figure 56, full time intervals for case A and B were used. Results that were obtained are presented in Table 28.

Table 28: Fitting parameters effect of superficial gas velocity

| | **Case A** | **Case B** | **Case C** | **Case D** | **Case E** | **Case F** | **Case G** | **Case H** |
|---|---|---|---|---|---|---|---|---|
| $A$ | 0.905 | 0.945 | 0.962 | 0.975 | 0.984 | 0.988 | 0.993 | 0.999 |
| $b$ | 0.941 | 2.041 | 2.615 | 3.096 | 3.459 | 4.039 | 4.039 | 4.285 |
| $R^2$ | 0.997 | 0.999 | 0.999 | 0.998 | 0.999 | 0.998 | 0.998 | 0.997 |

The dependence of mixing time to the superficial velocity is plotted in figure 53. In this figure, four different mixing-states are shown, 50% mixed, 75% mixed, 85% mixed and 99% mixed. Case A (0.4m/s) till case C (0.6m/s) steep trend was seen, while at higher velocities this trend flattens out.

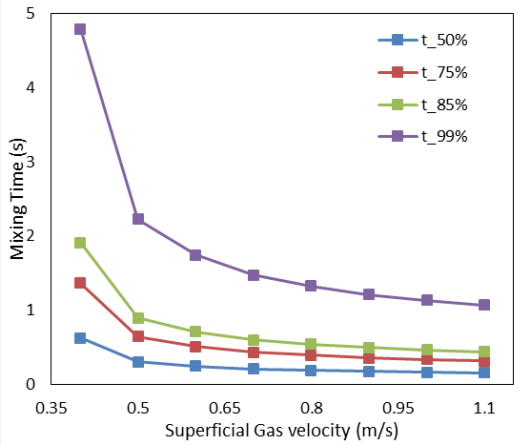


Figure 57: Mixing times for different velocities for several mix-states

This described trend is also visible during studying the effect of superficial gas velocity on heat transfer. At the lower velocities there is a steep decrease in the width of solid temperature distribution while the difference between the cases becomes small at high velocities.

## 6.5 Effect of restitution coefficient on solids mixing

As particle are exposed to heat, their physical properties may change. These properties may influence the fluidization regime and mixing properties. Especially higher temperature regions where hotspot tend to form; particles become softer.

Earlier research to the effect of this parameter was done by [30] and [17]. They found that a higher restitution coefficient leads to a decrease in bubble formation frequency. In this section, the effect of restitution coefficient on solids mixing rate is presented. The performed simulations are listed in Table 29 and Table 30.

Table 29: Tested cases for investigating the effect of restitution coefficient on solid mixing

| | Case A | Case B | Case C | Case D | Case E | Case F | Case G | Case H | Case I | Case J |
|---|---|---|---|---|---|---|---|---|---|---|
| $e_n$ | 0.60 | 0.70 | 0.80 | 0.85 | 0.90 | 0.95 | 0.96 | 0.97 | 0.98 | 0.99 |

Table 30: Simulation conditions for finding the effect of restitution coefficient on solid mixing

| Simulation conditions | | |
|---|---|---|
| Bed diameter | 0.6 | m |
| Bed height | 0.6 | m |
| Aspect ratio | 1 | - |
| Void fraction | 0.60 | - |
| Particle diameter | $9.875 \cdot 10^{-4}$ | m |
| Inlet gas temperature | 324 | K |
| Pressure | 101325 | Pa |
| Heat production | $6.7 \cdot 10^{5}$ | $W/m^3$ |
| Superficial gas velocity | 0.8 | m/s |
| Minimum fluidization velocity | 0.2455 | m/s |
| Coefficient of restitution | 0.60-0.99 | - |
| Wall coefficient of restitution | 0.97 | - |

First the effect of the restitution coefficient on the hydrodynamics was investigated, quantitative results are presented in the form of simulation snapshots in Figure 59. As can be seen in the pictures the bubbles become smaller with restitution coefficient. Also at higher restitution coefficient less red is visible, this color is the bubble phase fraction and instead a more uniform yellow and green color is visible.

Qualitative results are given in the form of a probability density function of the gas phase fraction (this PDF has been calculated according to equation (5.1)).

We found that the emulsion phase shrinks with an increase in the restitution coefficient. It was also observed that the intermediate phase becomes larger in simulations with larger restitution coefficients. In addition, the bubble phase becomes more noticeable in simulations with lower restitution coefficients.

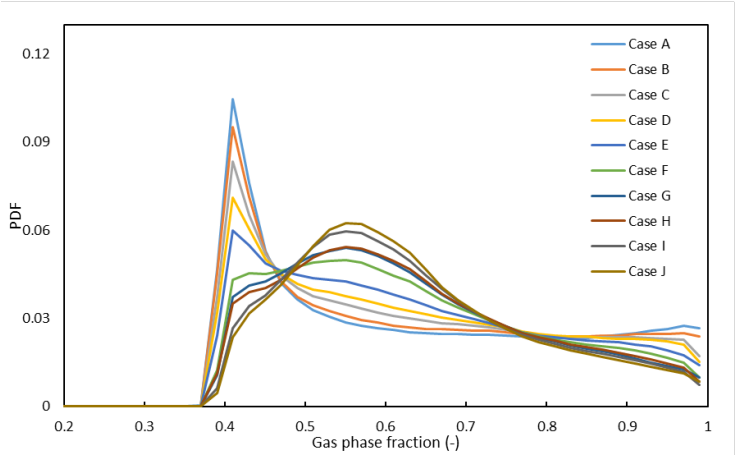


Figure 58: PDF of gas phase fraction in simulations with different restitution coefficient

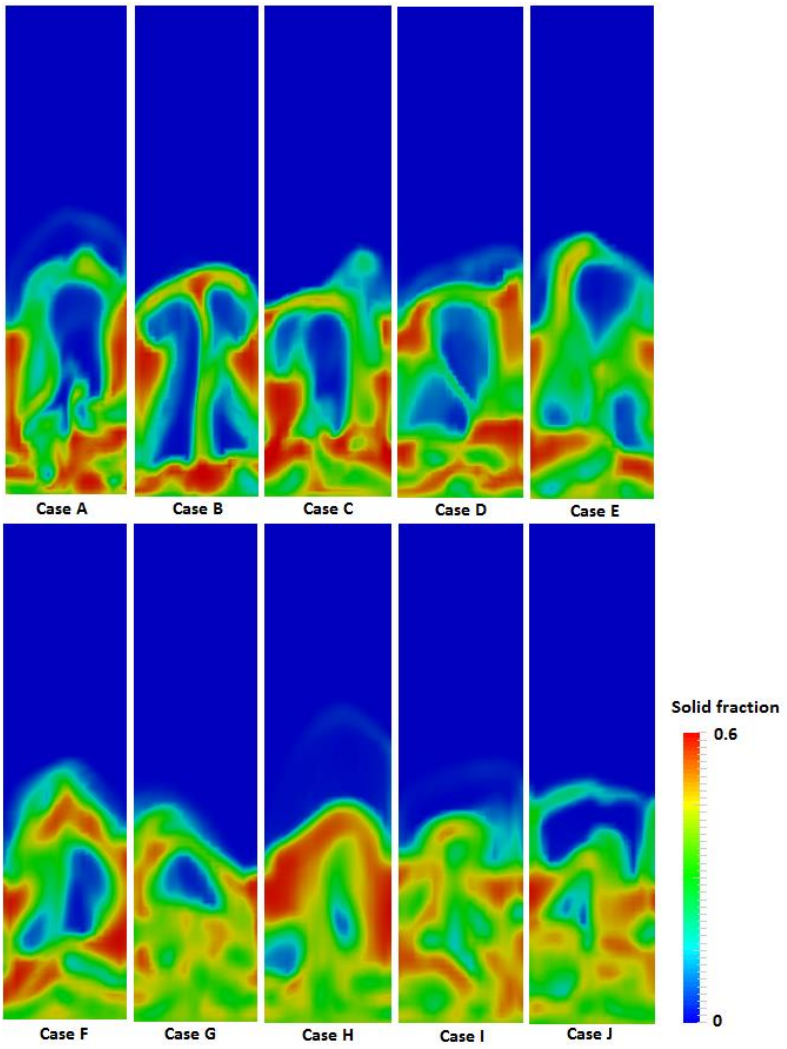


Figure 59: Effect of restitution coefficient, snapshot of a slice in the middle of the reactor

An explanation for this effect was given by [30] , due to the less ideal collisions more kinetic energy is dissipated when particles collide. Therefore, the velocity of a particle is lower after collision for particles with a lower restitution coefficient. This will lead to a particle configuration in which particles become closer packed.

It was seen in previous chapters that the mixing degree is directly connected to bubble formation in fluidized bed. Hence, we expect a better solid mixing at simulations with lower restitution coefficient. The mixing index for all the aforementioned simulations was calculated. For this calculation, five equal time intervals were used to obtain the averaged mixing index evolution. Results for the overall mixing index are plotted in Figure 60, and the results for horizontal and vertical mixing index are plotted in Figure 61 and Figure 62. It can be seen that the mixing occurs faster in cases with a lower restitution coefficient as expected.

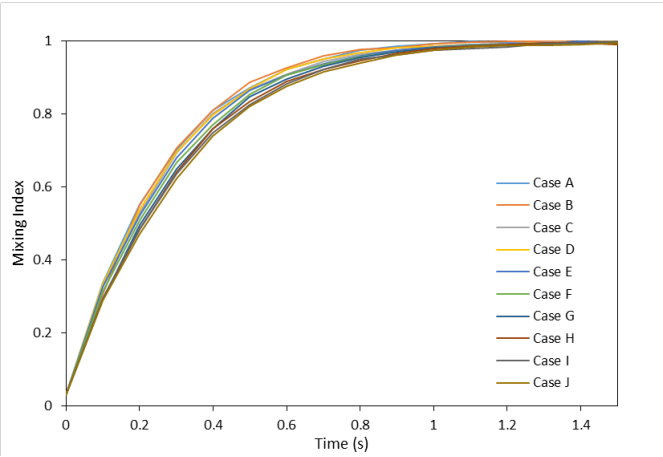


Figure 60: Effect of restitution coefficient on the overall mixing of particles

It was observed that mixing in the horizontal direction occurred slower compared to mixing in the vertical direction. Thus, horizontal mixing was dominant in determining of the overall mixing index.

Results for the mixing index were fitted to an exponential function (6.7), and mixing times for four cases (50%, 75%, 85% and 99%) have been plotted in Figure 63. This graph clearly shows that solid mixing is not highly sensitive to restitution coefficient.

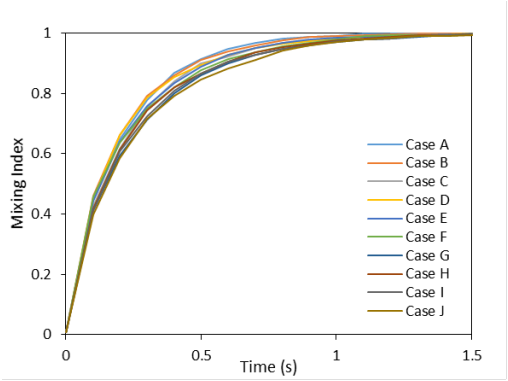


Figure 61: Effect of restitution coefficient on the horizontal mixing index

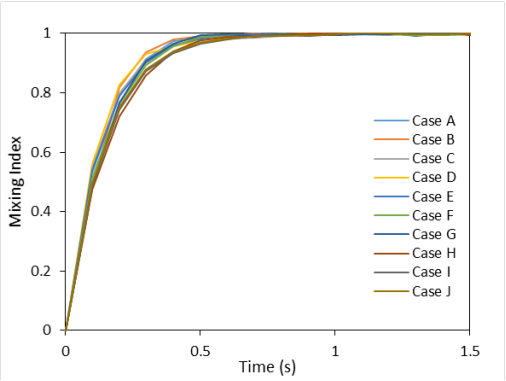


Figure 62: Effect of restitution coefficient on the vertical mixing index

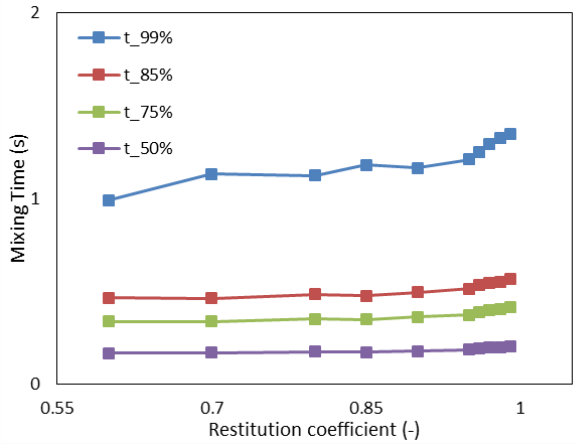


Figure 63: Effect of restitution coefficient on the solid mixing time

Furthermore, results for the pressure drop fluctuation are plotting in Figure 64. We observed a similar phenomenon but the fluctuations extent are less visible in this work compared to [30][17]. Therefore the standard deviations are calculated and are plotted in Figure 65. In [17] it is also stated that the fluctuations of the pressure should decrease with an increase in restitution coefficient. Results for the pressure drop fluctuation are plotted in Figure 64. In this case, only a small decrease is visible.

Qualitative results in the form of standard deviation for all cases are given in Table 31. Overall, a decreasing trend is visible in the standard deviation, but not as extreme as compared to [17]

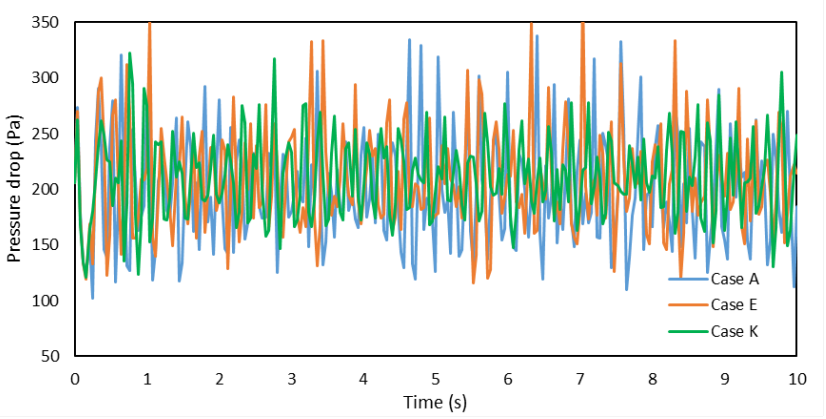


Figure 64: Effect of restitution coefficient on pressure drop

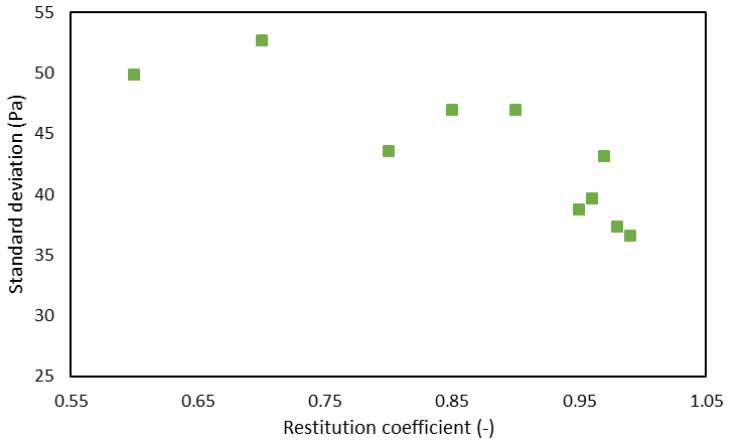


Figure 65: Effect of restitution coefficient on standard deviation on pressure fluctuations

Table 31: Effect of restitution coefficient on average pressure drop and pressure fluctuations

| | **Case A** | **Case B** | **Case C** | **Case D** | **Case E** | **Case F** | **Case G** | **Case H** | **Case I** | **Case K** |
|---|---|---|---|---|---|---|---|---|---|---|
| $e_n$ | 0.6 | 0.7 | 0.8 | 0.85 | 0.9 | 0.95 | 0.96 | 0.97 | 0.98 | 0.99 |
| average | 198.98 | 202.07 | 205.53 | 207.74 | 208.60 | 209.16 | 210.01 | 211.29 | 211.37 | 211.14 |
| Standard dev. | 49.89 | 52.70 | 43.61 | 47.01 | 47.014 | 38.78 | 39.67 | 43.12 | 37.37 | 36.58 |

Concluding, the restitution coefficient does have an influence on the hydrodynamics within a fluidized bed reactor. Lower restitution coefficient will result in more bubble formation due to the more inelastic collisions that take place. The influence of restitution coefficient on mixing properties is of minor influence comparing to the influence of superficial gas velocity.

# 7. Conclusions

Within this work the effect of superficial gas velocity in fluidized bed reactors is investigated. Therefore, with the aid of a two fluid model a 6 cm diameter bed is simulated. Conductive and convective heat transfer mechanism in this code were successfully verified by simple tests. Dependency on grid size and time step have been checked. It was chosen to use a particle dependent grid size of maximum 3 times $d_p$, with a time step of $1 \cdot 10^{-5}$ s.

In addition, the necessary routines for finding the tracers' motion were added to our in house TFM code. The movement of these tracers is based on solid flux at cell faces. A 'continuity satisfaction parameter' for verification purposes was introduced. It was found that this technique is capable of following the solid phase movement in a correct way.

Velocities between 0.4 – 1.1 m/s are tested. An increase in superficial gas velocity is coherent to more bubble formation in the bed. At this higher velocities less emulsion phase is visible and the intermediate and bubble phase are more present. With an increase in gas velocity a more uniform temperature distribution was observed. As the Nusselt number slightly decreases with increasing velocity, better heat transfer is therefore excluded as reason for this more uniform temperature. We found that the higher bubble formation causes faster solids mixing and circulation which consequently leads to a more uniform temperature throughout the bed. Mixing times for 99% mixing varies between 4.8s and 1.1s for the extreme cases.

The 6 cm bed was compared with a 12 cm bed simulation. The results of these simulations showed a similar trend compared to the 6cm bed simulation results. We found that solid temperature distribution becomes wider with increasing the bed diameter. The standard deviation of solid temperature for 12cm beds were roughly 2 times larger than its corresponding value in 6cm beds.

Besides that, the effect of superficial gas velocity and the influence of the restitution coefficient on the solids mixing was investigated. As collisions become less ideal (lower coefficient of restitution), more bubbles in the bed are observed where the emulsion phase is also more present. In the more ideal cases, the intermediate phase is the dominant phase. When particle collisions are less ideal, more energy is dissipated and the particle velocity is lower after collisions. As a consequence, particles are packed closer in some regions and there will be some empty (bubble) areas in other regions. Mixing rate is slightly decreases by this lower bubble formation.

# 8. Recommendations

Although the simulation conditions for capturing the heat transfer phenomenon were in agreement with the settings used by [1], but not all of these setting were realistic. For example, more realistic reaction kinetic and consequently more realistic solid heat production can be implemented into the code.

The low restitution coefficient, large bed size and relatively high operating pressure makes the simulations slow. Some of the planned simulations were not finished in time and they can be continued in the future.

The simulations for finding the effect of particle size on solid temperature distribution, a constant superficial gas velocity was used for all the simulations. Performing simulations with constant excess velocity or constant ratio between minimum fluidization and gas velocity can give further insight on the effect of this parameter in bed behavior.

As it is indicated, the method for finding solids mixing has some deficiencies like cell size sensitivity. It is therefore highly recommended to investigate this sensitivity in more detail.

Some of our results related to the effect of the restitution coefficient were different from previous researches. It is recommended to investigate this effect with more detail.

# Nomenclature

| Symbol | Name | Unit |
|---|---|---|
| $A$ | Inflow surface | [$m^2$] |
| $d$ | Particle diameter | [m] |
| $C_p$ | Heat capacity | [J/kg/K] |
| $e_n$ | Coefficient of restitution | [-] |
| $g$ | Gravitational acceleration | [m/s2] |
| $h$ | Thermal heat transfer coefficient | [W/m2/K] |
| $k$ | Thermal heat conductivity | [W/m/K] |
| $M$ | Molecular weight | [kg/mol] |
| $p$ | Pressure | [Pa] |
| $r$ | Radial coordinate | [m] |
| $t$ | Time | [s] |
| $T$ | Temperature | [K] |
| $u$ | Velocity | [m/s] |
| $v$ | Velocity | [m/s] |
| $V$ | Volume reactor | [$m^3$] |
| $z$ | Axial coordinate | [m] |
| Greek letters | | |
| $\beta$ | Interphase momentum coefficient | [$kg/m^3/s$] |
| $\gamma$ | Dissipation inelastic particle collisions | [$kg/m^3/s$] |
| $\varepsilon$ | Volume fraction | [$m^3/m^3$] |
| $\theta$ | Granular temperature | [$m^2/s^2$] |
| $\tau$ | Stress tensor | [Pa] |
| $\rho$ | Density | [$kg/m^3$] |
| $\mu$ | Viscosity | [Pa s] |
| Subscripts | | |
| $g$ | Gas | |
| $s$ | Solid | |
| $p$ | Particle | |
| $mf$ | Minimum fluidization | |
| Dimensionless numbers | | |
| Ar | Archnimedes number | |
| Re | Reynolds number | |
| $Nu$ | Nusselt number | |
| Pr | Prandtl | |
| Abbreviations | | |
| CSP | Continuity satisfaction parameter | |
| CSTR | Continuously stirred tank reactor | |
| DEM | Discrete element method | |
| KTGF | Kinetic theory of granular flow | |
| TFM | Two fluid model | |

# References


[1] Z. Li, M. van Sint Annaland, J. A. M. Kuipers, and N. G. Deen, "Effect of superficial gas velocity on the particle temperature distribution in a fluidized bed with heat production," *Chem. Eng. Sci.*, vol. 140, pp. 279–290, 2016.

[2] Y. Kaneko, T. Shiojima, and M. Horio, "DEM simulation of fluidized beds for gas-phase olefin polymerization," *Chem. Eng. Sci.*, vol. 54, no. 24, pp. 5809–5821, 1999.

[3] W. Kaminsky, "Production of Polyolefins by Metallocene Catalysts and Their Recycling by Pyrolysis," pp. 10–22, 2016.

[4] M. J. H. Khan, M. a. Hussain, Z. Mansourpour, N. Mostoufi, N. M. Ghasem, and E. C. Abdullah, "CFD simulation of fluidized bed reactors for polyolefin production – A review," *J. Ind. Eng. Chem.*, vol. 20, no. 6, pp. 3919–3946, 2014.

[5] McKenna, "Polyolefin Reaction Engineering – An Overview of Recent Developments," pp. 507–510, 2005.

[6] *High Pressure Fluidization*. .

[7] M. A. Van Der Hoef, M. V. S. Annaland, and J. A. M. Kuipers, "COMPUTATIONAL FLUID DYNAMICS FOR DENSE GAS-SOLID FLUIDIZED BEDS : A MULTI-SCALE MODELING STRATEGY," vol. 3, pp. 69–77, 2005.

[8] V. Verma, N. G. Deen, J. T. Padding, and J. a M. Kuipers, "Two-fluid modeling of three-dimensional cylindrical gas-solid fluidized beds using the kinetic theory of granular flow," *Chem. Eng. Sci.*, vol. 102, pp. 227–245, 2013.

[9] O. A. A. Ergun S., "Fluid flow through randomly packed columns and fluidized beds," *Ind. Eng. Chem.*, vol. 41, no. 6, pp. 1179–1184, 1949.

[10] C. Y. Wen and Y. H. Yu, "A generalized method for predicting the minimum fluidization velocity," *AIChE J.*, vol. 12, no. 3, pp. 610–612, 1966.

[11] D. J. Gunn, "Transfer of heat or mass to particles in fixed and fluidised beds," *Int. J. Heat Mass Transf.*, vol. 21, no. 4, pp. 467–476, 1978.

[12] S. Chapman and T. G. Crowling, *The mathematical theory of non-uniform gases*, 3rd editio. Cambrigde university press, 1970.

[13] D. Gidaspow, *Multiphase flow and Fluidization: Continuum and Kinetic theory description*. Academic press Boston, 1994.

[14] J. T. Jenkins and S. B. Savage, "A theory for the rapid flow of identical smooth, nearly elastic, spherical particles," *J. Fluid Mech.*, vol. 130, pp. 187–202, 1983.

[15] J. Ding and D. Gidaspow, "A bubbling fluidization model using kinetic theory of granular flow," *AIChE J.*, vol. 36, pp. 523–538, 1990.

[16] J. J. Nieuwland, M. . Veenendaal, J. A. M. Kuipers, and W. P. M. Van Swaaij, "Bubble formation at a single orifice in gas-fluidized beds," *Chem. Eng. Sci.*, vol. 51, pp. 4087–4102, 1996.

[17] M. Goldschmidt, *Hydrodynamic Modelling of Fluidised Bed Spray Granulation*. 2001.

[18] Vikrant Verma, "Cylindrical fluidized beds; modeling, simulation, and experimental study," TU/e, 2014.

[19] H. S. C. J. C. Jaeger, “Conduction of Heat in Solids.” 1959.

[20] E. J. G. Eriksson and T. F. McKenna, “Heat-transfer phenomena in gas-phase olefin polymerization using computational fluid dynamics,” *Ind. Eng. Chem. Res.*, vol. 43, no. 23, pp. 7251–7260, 2004.

[21] Y. Che, Z. Tian, Z. Liu, R. Zhang, Y. Gao, E. Zou, S. Wang, and B. Liu, “A CFD-PBM model considering ethylene polymerization for the flow behaviors and particle size distribution of polyethylene in a pilot-plant fluidized bed reactor,” *Powder Technol.*, vol. 286, pp. 107–123, 2015.

[22] H. K.Y. Choi, Ray, “Polymerization of Olefins through Heterogeneous Catalysis. 11. Kinetics of Gas Phase Propylene Polymerization with Ziegler-Nat t a Cat a 1,” vol. 30, pp. 1065–1081, 1985.

[23] W. Yang, “Modification and re-interpretation of Geldart ’ s classification of powders,” vol. 171, pp. 69–74, 2007.

[24] J. Chmelar, P. Matuska, T. Gregor, M. Bobak, F. Fantinel, and J. Kosek, “Softening of polyethylene powders at reactor conditions,” *Chem. Eng. J.*, vol. 228, pp. 907–916, 2013.

[25] A. E. Abasaeed, “Modeling of Fluidized Bed Reactors for the Polymerization Reaction of Ethylene and Propylene,” vol. 6, pp. 121–134, 1998.

[26] J. B. P. S. And and T. F. L. McKenna, *Polyolefin reaction engineering*. Wiley, 2007.

[27] S. Cloete, A. Zaabout, S. T. Johansen, M. van Sint Annaland, F. Gallucci, and S. Amini, “The generality of the standard 2D TFM approach in predicting bubbling fluidized bed hydrodynamics,” *Powder Technol.*, vol. 235, pp. 735–746, 2013.

[28] Y. Behjat, S. Shahhosseini, and S. H. Hashemabadi, “CFD modeling of hydrodynamic and heat transfer in fluidized bed reactors,” *Int. Commun. Heat Mass Transf.*, vol. 35, no. 3, pp. 357–368, 2008.

[29] M. a. Dehnavi, S. Shahhosseini, S. H. Hashemabadi, and S. M. Ghafelebashi, “CFD simulation of hydrodynamics and heat transfer in gas phase ethylene polymerization reactors,” *Int. Commun. Heat Mass Transf.*, vol. 37, no. 4, pp. 437–442, 2010.

[30] B. P. B. Hoomans, J. a. M. Kuipers, W. J. Briels, and W. P. M. van Swaaij, “Discrete particle simulation of bubble and slug formation in a two-dimensional gas-fluidised bed: A hard-sphere approach,” *Chem. Eng. Sci.*, vol. 51, no. 1, pp. 99–118, 1996.

[31] C. Twente, “Characterizing solids mixing in DEM simulations W. Godlieb, N.G. Deen and J.A.M. Kuipers,” no. 272, 2007.

# Acknowledgement

I have been working nine months on finishing my master thesis, at the start I had a difficult time, luckily I had enough people around me to help me out and I would like to thank them.

A special word of thanks will go to my daily supervisor Mohammad Banaei MSc. I would like to thank him for everything he taught me, his creative input, discussions, for the support and the good times we had. I wish him good luck with finishing his PhD.

Further, I want to thank prof. dr. ir. J.A.M Kuipers for the possibility to do a graduation project within the SMR group. I also want to thank prof. dr. ir. N.G. Deen as a supervisor and his helpful input. I would also like to thank dr. ir. J. van der Schaaf for joining the examination committee.

I want to thank all my friends and family for the (social) support during the last 9 months. Without them I would not be able to come this far.

# Appendixes

## Appendix A: Two fluid model equation

Extended momentum equations

*Radial direction:*

$$\frac{\partial\left(\varepsilon_s\rho_s u_{s,r}\right)}{\partial t}+\frac{1}{r}\frac{\partial\left(r\varepsilon_s\rho_s u_{s,r}u_{s,r}\right)}{\partial r}+\frac{1}{r}\frac{\partial\left(r\varepsilon_s\rho_s u_{s,\theta}u_{s,r}\right)}{\partial r}-\frac{\rho_s\varepsilon_s\left(u_{s,\theta}u_{s,\theta}\right)}{r}+\frac{\partial\left(\varepsilon_s\rho_s u_{s,z}u_{s,r}\right)}{\partial z}=$$
$$-\varepsilon_s\frac{\partial p}{\partial r}-\frac{\partial p_s}{\partial r}-\left(\frac{1}{r}\frac{\partial\left(\varepsilon_s r\tau_{s,rr}\right)}{\partial r}+\frac{1}{r}\frac{\partial\left(\varepsilon_s\tau_{s,\theta r}\right)}{\partial\theta}-\frac{\varepsilon_s\tau_{s,\theta\theta}}{r}+\frac{\partial\left(\varepsilon_s\tau_{s,zr}\right)}{\partial z}\right)+\beta\left(u_{g,r}-u_{s,r}\right)+\varepsilon_s\rho_s g_r$$

*Azimuthal direction:*

$$\frac{\partial\left(\varepsilon_s\rho_s u_{s,\theta}\right)}{\partial t}+\frac{1}{r}\frac{\partial\left(r\varepsilon_s\rho_s u_{s,r}u_{s,\theta}\right)}{\partial r}+\frac{1}{r}\frac{\partial\left(r\varepsilon_s\rho_s u_{s,\theta}u_{s,\theta}\right)}{\partial\theta}+\frac{\partial\left(\varepsilon_s\rho_s u_{s,z}u_{s,\theta}\right)}{\partial z}-\frac{\rho_s\varepsilon_s u_{s,\mathrm{r}}u_{s,\theta}}{r}=$$
$$-\varepsilon_s\frac{1}{r}\frac{\partial p}{\partial\theta}-\frac{1}{r}\frac{\partial p_s}{\partial\theta}-\left(\frac{1}{r^2}\frac{\partial\left(\varepsilon_s r^2\tau_{s,r\theta}\right)}{\partial r}+\frac{1}{r}\frac{\partial\left(\varepsilon_s\tau_{s,\theta\theta}\right)}{\partial\theta}+\frac{\partial\left(\varepsilon_s\tau_{s,z\theta}\right)}{\partial z}\right)+\beta\left(u_{g,r\theta}-u_{s,\theta}\right)+\varepsilon_s\rho_s g_\theta$$

*Axial direction*

$$\frac{\partial\left(\varepsilon_s\rho_s u_{s,\mathrm{z}}\right)}{\partial t}+\frac{1}{r}\frac{\partial\left(r\varepsilon_s\rho_s u_{s,\mathrm{r}}u_{s,\mathrm{z}}\right)}{\partial r}+\frac{1}{r}\frac{\partial\left(r\varepsilon_s\rho_s u_{s,\theta}u_{s,\mathrm{z}}\right)}{\partial\theta}+\frac{\partial\left(\varepsilon_s\rho_s u_{s,\mathrm{z}}u_{s,z}\right)}{\partial z}-\frac{\rho_s\varepsilon_s u_{s,\mathrm{r}}u_{s,\theta}}{r}=$$
$$-\varepsilon_s\frac{\partial p}{\partial z}-\frac{\partial p_s}{\partial z}-\left(\frac{1}{r}\frac{\partial\left(\varepsilon_s r\tau_{s,rz}\right)}{\partial r}+\frac{1}{r}\frac{\partial\left(\varepsilon_s\tau_{s,\theta z}\right)}{\partial\theta}+\frac{\partial\left(\varepsilon_s\tau_{s,\mathrm{zz}}\right)}{\partial z}\right)+\beta\left(u_{g,r\theta}-u_{s,\theta}\right)+\varepsilon_s\rho_s g_z$$

The gas phase equations can be obtained by replace the *s* subscripts by *g*. One should keep in mind for the gas phase the solid pressure gradient can be excluded.

# Appendix B: Discretization fixed bed convection verification

*Gas temperature*

$$\varepsilon_g C_{p,g}\rho_g \frac{\partial T_{g,z}}{\partial t} = -u_z \varepsilon_g C_{p,g}\rho_g \frac{\partial T_{g,z}}{\partial z} + ha_s \left(T_{p,z} - T_{g,z}\right)$$

$$\frac{\partial T_{g,z}}{\partial t} = -u_z \frac{\partial T_{g,z}}{\partial z} + \frac{ha_s}{\varepsilon_g C_{p,g}\rho_g}\left(T_{p,z} - T_{g,z}\right)$$

$$\frac{T_{g,i}^{n+1} - T_{g,i}^{n}}{\Delta t} = -u_z \frac{T_{g,\mathrm{i}}^{n+1} - T_{g,\mathrm{i}-1}^{n+1}}{\Delta z} + \frac{ha_s}{\varepsilon_g C_{p,g}\rho_g}\left(T_{p,i}^{n+1} - T_{g,i}^{n+1}\right)$$

$$\frac{T_{g,i}^{n+1} - T_{g,i}^{n}}{\Delta t} = -u_z \frac{T_{g,\mathrm{i}}^{n+1} - T_{g,\mathrm{i}-1}^{n+1}}{\Delta z} + \frac{ha_s}{\varepsilon_g C_{p,g}\rho_g}\left(T_{p,i}^{n+1} - T_{g,i}^{n+1}\right)$$

$$T_{g,i}^{n+1}\left(\frac{1}{\Delta t} + \frac{u_z}{\Delta z} + \frac{ha_s}{\varepsilon_g C_{p,g}\rho_g}\right) - \frac{ha_s}{\varepsilon_g C_{p,g}\rho_g} T_{p,i}^{n+1} = \frac{1}{\Delta t} T_{g,i}^{n} + \frac{u_z}{\Delta z} T_{g,\mathrm{i}-1}^{n+1}$$

*Solid temperature*

$$\varepsilon_s C_{p,p}\rho_p \frac{\partial T_p}{\partial t} = ha_s \left(T_{g,z} - T_p\right) + \varepsilon_s \dot{q}_p$$

$$\varepsilon_s C_{p,p}\rho_p \frac{\partial T_p}{\partial t} = ha_s \left(T_{g,z} - T_p\right) + \varepsilon_s \dot{q}_p$$

$$\frac{\partial T_p}{\partial t} = \frac{ha_s}{\varepsilon_s C_{p,p}\rho_p}\left(T_{g,z} - T_p\right) + \frac{\dot{q}_p}{C_{p,p}\rho_p}$$

$$\frac{T_p^{n+1} - T_p^{n}}{\Delta t} = \frac{ha_s}{\varepsilon_s C_{p,p}\rho_p}\left(T_{g,i}^{n+1} - T_p^{n+1}\right) + \frac{\dot{q}_p}{C_{p,p}\rho_p}$$

$$T_p^{n+1}\left(\frac{1}{\Delta t} + \frac{ha_s}{\varepsilon_s C_{p,p}\rho_p}\right) - \frac{ha_s}{\varepsilon_s C_{p,p}\rho_p} T_{g,i}^{n+1} = \frac{1}{\Delta t} T_p^{n} + \frac{\dot{q}_p}{C_{p,p}\rho_p}$$

# Appendix C: Discretization initial temperature

Gas phase

$$\varepsilon_g \rho_g c_{p,g} V \frac{\partial T_g}{\partial t} = u_g A \rho_g c_{p,g} \left(T_{g,in} - T_g\right) + \alpha \, \mathrm{a}_s \, V \left(T_p - T_g\right)$$

$$\frac{\partial T_g}{\partial t} = \frac{u_g \left(T_{g,in} - T_g\right)}{\varepsilon_g H} + \frac{\alpha \, \mathrm{a}_s \left(T_p - T_g\right)}{\varepsilon_g \rho_g c_{p,g}}$$

$$\frac{T_g^{n+1} - T_g^n}{\Delta t} = \frac{u_g \left(T_{g,in} - T_g^{n+1}\right)}{\varepsilon_g H} + \frac{\alpha \, \mathrm{a}_s \left(T_p^n - T_g^{n+1}\right)}{\varepsilon_g \rho_g c_{p,g}}$$

$$T_g^{n+1} \left[1 + \frac{\Delta t u_g}{\varepsilon_g H} + \frac{\Delta t \alpha \, \mathrm{a}_s}{\varepsilon_g \rho_g c_{p,g}}\right] = T_g^n + \frac{\Delta t u_g}{\varepsilon_g H} T_{g,in} + \frac{\Delta t \alpha \, \mathrm{a}_s}{\varepsilon_g \rho_g c_{p,g}} T_p^n$$

$$A = \frac{\Delta t u_g}{\varepsilon_g H}$$

$$B = \frac{\Delta t \alpha \, \mathrm{a}_s}{\varepsilon_g \rho_g c_{p,g}}$$

$$T_g^{n+1} = \frac{T_g^n + A T_{g,in} + B T_p^n}{1 + A + B}$$

Particle phase

$$\varepsilon_p \rho_p c_{p,p} V \frac{\partial T_p}{\partial t} = \alpha \, \mathrm{a}_s \, V \left(T_g - T_p\right) + \varepsilon_s V q$$

$$\frac{\partial T_p}{\partial t} = \frac{\alpha \, \mathrm{a}_s \left(T_g - T_p\right)}{\varepsilon_p \rho_p c_{p,p}} + \frac{q}{\rho_p c_{p,p}}$$

$$\frac{T_p^{n+1} - T_p^n}{\Delta t} = \frac{\alpha \, \mathrm{a}_s \left(T_g^n - T_p^{n+1}\right)}{\varepsilon_p \rho_p c_{p,p}} + \frac{q}{\rho_p c_{p,p}}$$

$$T_p^{n+1} \left[1 + \frac{\Delta t \alpha \, \mathrm{a}_s}{\varepsilon_p \rho_p c_{p,p}}\right] = T_p^n + \frac{\Delta t \alpha \, \mathrm{a}_s \, T_g^n}{\varepsilon_p \rho_p c_{p,p}} + \frac{\Delta t q}{\rho_p c_{p,p}}$$

$$C = \frac{\Delta t \alpha \, \mathrm{a}_s}{\varepsilon_p \rho_p c_{p,p}}$$

$$D = \frac{\Delta t q}{\rho_p c_{p,p}}$$

$$T_p^{n+1} = \frac{T_p^n + C T_g^n + D}{1 + C}$$